

# Retrieval of optical and physical properties of African dust from multi-wavelength Raman lidar measurements during the “SHADOW” campaign in Senegal

I. Veselovskii<sup>1,2</sup>, P. Goloub<sup>3</sup>, T. Podvin<sup>3</sup>, V. Bovchaliuk<sup>3</sup>, Y. Derimian<sup>3</sup>, P. Augustin<sup>4</sup>, M. Fourmentin<sup>4</sup>, D. Tanre<sup>3</sup>, M. Korenskiy<sup>1,5</sup>, D.N. Whiteman<sup>6</sup>, A. Diallo<sup>7</sup>, T. Ndiaye<sup>7</sup>, A. Kolgotin<sup>1</sup>, O. Dubovik<sup>3</sup>

<sup>1</sup>*Physics Instrumentation Center of GPI, Troitsk, Moscow, 142190, Russia*

<sup>2</sup>*Joint Center for Earth Systems Technology, UMBC, Baltimore, MD, USA*

<sup>3</sup>*Laboratoire d'Optique Atmosphérique, Université de Lille-CNRS, 59650, Villeneuve d'Ascq, France*

<sup>4</sup>*Laboratoire de Physico-chimie de l'atmosphère, Université du littoral côte d'Opale, France*

<sup>5</sup>*Far Eastern Federal University, Russia*

<sup>6</sup>*NASA GSFC, Greenbelt, MD 20771, USA*

<sup>7</sup>*Institut de Recherche pour le Développement, Dakar, Sénégal*

## 1 **ABSTRACT**

2 West Africa and the adjacent oceanic regions are very important locations for studying  
3 dust properties and their influence on weather and climate. The SHADOW (Study of SaHaran  
4 Dust Over West Africa) campaign is performing a multi-scale and multi-laboratory study of  
5 aerosol properties and dynamics using a set of in situ and remote sensing instruments at an  
6 observation site located at IRD (Institute for Research and Development) Center, Mbour,  
7 Senegal (14°N, 17°W). In this paper, we present the results of lidar measurements performed  
8 during the first phase of SHADOW which occurred in March-April, 2015. The multiwavelength  
9 Mie-Raman lidar acquired  $3\beta+2\alpha+1\delta$  measurements during this period. This set of measurements  
10 has permitted particle intensive properties such as extinction and backscattering Ångström  
11 exponents (BAE) for 355/532 nm wavelengths corresponding lidar ratios and depolarization ratio  
12 at 532 nm to be determined. The mean values of dust lidar ratios during the observation period  
13 were about 53 sr at both 532 nm and 355 nm, which agrees with the values observed during the  
14 SAMUM 1 and SAMUM 2 campaigns held in Morocco and Cape Verde in 2006, 2008. The  
15 mean value of particle depolarization ratio at 532 nm was  $30\pm 4.5\%$ , however during strong dust  
16 episodes this ratio increased to  $35\pm 5\%$ , which is also in agreement with the results of the

1 SAMUM campaigns. The backscattering Ångström exponent during the dust episodes decreased  
2 to  $\sim -0.7$ , while the extinction Ångström exponent though being negative, was greater than  $-0.2$ .  
3 Low values of BAE can likely be explained by an increase in the imaginary part of the dust  
4 refractive index at 355 nm compared to 532 nm. The dust extinction and backscattering  
5 coefficients at multiple wavelengths were inverted to the particle microphysics using the  
6 regularization algorithm and the model of randomly oriented spheroids. The analysis performed  
7 has demonstrated that the spectral dependence of the imaginary part of the dust refractive index  
8 may significantly influence the inversion results and should be taken into account.

9

## 10 **1. INTRODUCTION**

11 The impact of desert dust emitted into atmosphere on the Earth's radiation budget is the  
12 subject of intense research (Sokolik and Toon, 1996; Balkanski et al., 2007; Mahowald et al.,  
13 2010; Formenti et al., 2011, 2014). Due to the wind patterns involved, dust can be transported far  
14 away from the main source regions in Africa and Asia allowing dust to be distributed in varying  
15 amounts all over the globe. North Africa is the largest source of dust in the world and several  
16 field campaigns have been conducted to evaluate dust particle microphysical properties over  
17 Western Africa and to study long range transport of Saharan dust (Reid et al., 2003; Tanre et al.,  
18 2003; Redelsperger et al., 2006; Haywood et al., 2008; McConnell et al., 2008). During these  
19 campaigns, dust particles were studied via aircraft, ground sampling and using sun photometer  
20 measurements. However, vertical distribution of dust has received little attention even though  
21 dust vertical structure is critical for an improved understanding of dust advection, transport and  
22 dust-cloud interactions. The commonly used instrument to evaluate the height profile of dust  
23 particle properties is the aerosol lidar. The numerous measurements performed in Europe,  
24 America and Asia with multiwavelength Raman and HSRL lidar systems have resulted in a  
25 significant amount of information about the vertical distribution of dust intensive properties,  
26 such as depolarization, lidar ratios, extinction and backscattering Ångström exponents (Sakai et  
27 al., 2003; De Tomasi et al., 2003; Shimizu et al., 2004; Mona et al., 2006; Papayannis et al.,  
28 2008; Xie et al., 2008; Ansmann et al., 2012; Burton et al., 2014; Nisantzi et al., 2015). However  
29 these measurements were mostly performed at a significant distance from the source area, so the  
30 dust particles were aged due to mixing with local aerosols and coating with soluble aerosol

1 species (Li et al., 2009) and may not have well represented the characteristics of the dust upon  
2 initial emission.

3 To analyze the properties of pure dust measurements near the source regions are needed.  
4 Such measurements of Saharan dust were performed during the SAMUM1 and SAMUM2  
5 experiments using the assembly of Raman and HSRL lidars (Ansmann et al., 2011). During  
6 those measurements the dust episodes and more complicated events, when the dust and smoke  
7 layers occurred simultaneously, were studied (Tesche et al., 2009a,b; 2011; Esselborn et al.,  
8 2009). However, for the estimation of aerosol radiative forcing not only the particle intensive  
9 parameters, but also their microphysical properties, such as size, concentration and the complex  
10 refractive index (CRI) are needed. An estimation of the vertical distribution of particle  
11 microphysics can be achieved, for example, by combining lidar and sun photometer  
12 measurements; a review of such studies can be found in a recent publication (Binietoglou et al.,  
13 2015). However in these retrievals the mean radii and refractive indices of particles in the fine  
14 and the coarse mode are assumed to be height independent, and only particle volume in each of  
15 the modes is permitted to vary. Such assumptions may become invalid when aerosol layers of  
16 different origins occur.

17 The alternative approach to evaluating the vertical distribution of dust properties is to  
18 estimate the particle properties from lidar measurements only. Raman (or HSRL)  
19 multiwavelength lidars based on a tripled Nd:YAG laser are able to provide three particle  
20 backscattering and two extinction coefficients (so called  $3\beta+2\alpha$  dataset). Different techniques  
21 have been considered to invert these measurements into particle microphysics (Ansmann and  
22 Müller, 2005), but the main issue is small number of input measurements (typically five),  
23 compared to the numerous parameters needed for describing the aerosol microphysical  
24 properties. This implies that the inverse problem is underdetermined and that numerous solutions  
25 may reproduce the input measurements with similar accuracy. This family of solutions can be  
26 localized by applying constraints to the "search space", i.e. limiting the range of particle radii and  
27 refractive indices considered. The additional assumption usually made is that the refractive index  
28 is spectrally independent and identical over the whole size range (Müller et al., 1999;  
29 Veselovskii et al., 2002). Such an approach has proved to be efficient for aerosol particle size  
30 distributions (PSD) with a predominant fine mode as, for example, in the case of biomass  
31 burning aerosols (Müller et al., 2005; Veselovskii et al., 2015). However, in the case of dust the

1 inversion of lidar measurements becomes more challenging since the dust PSD contains a strong  
2 coarse mode with particle radii extending up to  $\sim 15 \mu\text{m}$  and the estimation of properties for such  
3 big particles is less accurate when measurements are only performed in the wavelength range of  
4 355-1064 nm. Moreover, dust particles are of irregular shape and Mie theory is thus not  
5 applicable for computations of their scattering properties. Also, the imaginary part of the  
6 refractive index (RI) of dust is spectrally dependent, with a strong enhancement of the absorption  
7 in the UV region (Patterson et al., 1977). And finally, particles in the fine and coarse mode may  
8 have different origin, so the size dependence of the refractive index should also be considered.  
9 The complexity of the problem outlined above demands the use of assumptions and  
10 simplifications in the retrieval algorithms.

11 A widely used model for treating irregularly shaped particles is the one used in the  
12 operational AERONET algorithm that mimics dust scattering properties with an assembly of  
13 randomly oriented spheroids (Mishchenko et al., 1997; Dubovik et al., 2006). For typical dust  
14 PSDs the AERONET model provides lidar and depolarization ratios which agrees reasonably  
15 well with observed values (Wiegner et al., 2009). The first attempts to invert lidar dust  
16 measurements into particle microphysics using the spheroids model were recently made  
17 (Veselovskii et al., 2010; Di Girolamo et al., 2012; Papayannis et al., 2012) but were applied to  
18 lofted layers of aged dust over Europe. The only test of the spheroidal model relevant to pure  
19 dust was performed by using the data acquired during the SAMUM-1 and SAMUM-2 campaigns  
20 (Müller et al., 2013). Results indicate that the effective radii derived from lidar measurements are  
21 in reasonable agreement with the values provided by AERONET and airplane sampling, while  
22 differences are significant for the refractive index.

23 The application of spheroids to the analysis of lidar dust observations is an important step  
24 forward when compared to the spherical particle approximation of Mie theory. Still we should  
25 keep in mind that spheroid model was not specifically designed for lidar applications where  
26 scattering in the backward direction is considered. For instance, as previously discussed  
27 (Gasteiger et al., 2011; Müller et al., 2013) the spheroidal model has difficulty in reproducing  
28 depolarization ratios ( $\delta$ ) greater than 30%, values that are representative for pure dust. When  
29 using the spheroidal model, such high depolarization ratios can only be obtained when the real  
30 ( $m_R$ ) and imaginary ( $m_i$ ) parts of the refractive index are less than 1.5 and 0.005, respectively  
31 (Dubovik et al., 2006), even though coincident in situ measurements of dust report higher values

1 (Kandler et al., 2011). To investigate these issues, more measurements near the dust origin  
2 source and more tests of suitable inversion schemes are needed.

3 West Africa and the adjacent oceanic regions are very important locations for studying  
4 dust properties and their influence on weather and climate. The SHADOW (Study of SaHaran  
5 Dust Over West Africa) campaign is performing a multi-scale and multi-laboratory study of  
6 aerosol properties and dynamics using a set of in situ and remote sensing instrumentation (multi-  
7 wavelength Raman LIDAR, Wind-LIDAR, nephelometer, aethalometer, sun/lunar photometer,  
8 airborne sunphotometer, optical particle counter) in the framework of the CaPPA (Chemical and  
9 Physical Processed in The Atmosphere) project (<http://www.labex-cappa.fr/>). The objective of  
10 the experiment is to report the optical, chemical and physical properties of the aerosols as well as  
11 the source apportionment in a location where aerosol loading can be very large and aerosol type  
12 depends on the season. Two enhanced observing periods of 7 weeks are considered: March-April  
13 2015 when dust due to the Harmattan, which is a dry trade wind that transports dust laden air  
14 from the Sahara to West Africa (Schwanghart and Schütt, 2008) is dominant, and December  
15 2015-January 2016 when dust and carbonaceous aerosols resulting from fire activities are in  
16 variable proportion and transported at different altitudes. Other types of aerosols can also be  
17 present such as sulfates from nearby urban areas or maritime aerosols depending on the air mass  
18 flow. The mixed state of these various chemical components results in different radiative  
19 properties of the aerosols.

20 We hereinafter focus our study on multiwavelength Mie-Raman lidar measurements  
21 performed during the first phase of the SHADOW campaign for the period 8 March - 24 April  
22 2015. During this period approximately 40 day- and night-time measurement sessions were  
23 performed and numerous strong dust episodes were observed. Those lidar observations are used  
24 for the analysis of the vertical distribution of the dust intensive and microphysical properties. In  
25 section 2 we describe the lidar equipment and the meteorological characteristics of the  
26 observation site. Section 3 presents day-to-day variation of dust properties and examples of  
27 vertical distribution of dust intensive parameters. The results of inversion of lidar measurements  
28 into particle microphysics are given in section 4.

## 29 30 31 **2. INSTRUMENTATION AND METEOROLOGY OF THE OBSERVATION SITE**

## 2.1 Instrumentation

The site is located at the Institute for Research and Development (IRD) Center, Mbour, Senegal (14°N, 17°W). Aerosol observations with the AERONET sun photometer and micropulse lidar have been performed since 1996 and 2005 respectively. Moreover, for the period of the SHADOW experiment, two additional lidar systems were installed: a Doppler wind lidar and a multiwavelength Mie-Raman lidar.

### *Doppler lidar*

The wind field within the lower troposphere (<5 km) was measured by an eye safe scanning wind lidar (Windcube WLS 100) manufactured by the LEOSPHERE company (www.leosphere.com). This pulsed Doppler lidar operates at 1543 nm with a repetition rate of 10 kHz and uses a heterodyne technique to measure the Doppler shift of laser radiation backscattered by aerosols. Simultaneous measurements of radial wind speed and aerosol backscatter provides information on both aerosol layer stratification and the dynamics of the lower troposphere (Thobois and Soderholm, 2015). More technical details are given by (Kumer et al., 2014; Ruchith and Ernest Raj, 2015).

During this experiment, continuous monitoring of the wind field in the range from 100 m to 5 km with 50 m range resolution was performed. The total scanning cycle included two 180° scans in the vertical plane along East/West and South/North axes with 1° resolution, 360° azimuthal scan with 2° resolution at 5° elevation angle, and line of sight (LOS) profiles at 75° elevation in the four cardinal directions. The duration of the total cycle was approximately 10 minutes. The combination of LOS sequences is used in order to determine the three components of the wind vector vertical profile relying on the Doppler Beam Swinging (DBS) technique (Browning and Wexler, 1968).

### *Multiwavelength Mie-Raman lidar*

The LILAS multiwavelength Mie-Raman lidar is based on a tripled Nd:YAG Spectra Physics INDI laser with a 20 Hz repetition rate, and pulse energy of 90/100/100 mJ at 355/532/1064 nm. The backscattered light is collected by a 40-cm aperture Newtonian telescope, which is inclined at an angle of 47 degrees to the horizon. Measurements were performed from inside the IRD building through a window and 47 deg to horizon was the maximal angle possible. The outputs of the detectors (R1924, R9880 PMTs for 355 nm-532 nm spectral range

1 and APD for 1064 nm) are recorded at 7.5 m range resolution using Licel transient recorders that  
2 incorporate both analog and photon-counting electronics. The full geometrical overlap of the  
3 laser beam and the telescope FOV is achieved at 800 m -1400 m range depending on FOV used.  
4 The system is designed for simultaneous detection of elastic and Raman backscatter signals and  
5 thus provides three particle backscattering and two extinction coefficients along with  
6 depolarization ratio at 532 nm (so called  $3\beta+2\alpha+1\delta$  set). For the calibration of depolarization  
7 measurements, the so called  $\pm 45^\circ$  method, (Freudenthaler et al., 2009) was used. The relative  
8 uncertainty of depolarization measurements due to calibration is estimated as  $\pm 15\%$ . Acquiring  
9 Raman backscatter at 408 nm permits profiling the water vapor mixing ratio (WVMR)  
10 (Whiteman et al., 1992). For calibration of the WVMR, radiosonde launches from the Dakar  
11 airport, located  $\sim 70$  km from Mbour, were used. The large separation between the lidar and  
12 radiosonde locations prevented an accurate calibration of the WVMR so the WVMR data were  
13 used mainly to monitor the relative change of the water vapor content. To improve the system  
14 capability for measurements of particle extinction coefficient at 532 nm, rotational Raman (RR)  
15 scattering was used instead of vibrational nitrogen Raman scattering at 608 nm (Veselovskii et  
16 al., 2015). For each profile, 4000 laser pulses were accumulated so the temporal resolution of the  
17 measurements was approximately 3 minutes. The backscattering coefficients and depolarization  
18 ratio were calculated with range resolution 7.5 m (corresponding height resolution 5.5.m).  
19 Resolution of extinction coefficient measurements varied with height from 50 m (at 1000 m) to  
20 125 m at (at 7000 m).

## 21 **2.2. Meteorological characteristics of the observation site**

22 During the experimental period, complex lower tropospheric ( $< 3000$  m) stratification  
23 was frequently observed over the site. As we will show, this was likely due to the different  
24 origins of air masses including tropical circulation arriving from maritime (moist) and  
25 continental trade winds (dry). Moreover, a transitional form of these two main trade winds were  
26 observed and described as Continentalized Maritime Trade winds (CMT). Thus, during the  
27 SHADOW campaign, the wind fields over the site were characterized by Maritime Trades (NW),  
28 Continentalized Maritime Trades (N to NNE), Sea breezes (WSW to WNW) and Continental  
29 trades (Harmattan), the latter indicates the presence of air mass advection coming from the  
30 northeastern/eastern drylands. One particularity of this site was the presence of recurrent Low  
31 Level Jets (NNW to ENE) which occurred during approximately 69% of the campaign period

1 and were located below 1000 m in elevation. The transport paths of different stratified air masses  
2 were studied by using back trajectories from the NOAA HYSPLIT model (Stein et al., 2015).

3 Fig 1-4 were derived from joint use of wind and Raman lidar measurements on the night  
4 of 15-16 April 2015 and illustrate the aerosol stratification that frequently characterized the  
5 observation site. For the period from 23:00 UTC to 7:00 UTC on 15-16 April 2015 night, the  
6 time-height sections of the logarithmic range corrected signal (LRCS) is shown in Fig.1, while  
7 Fig.2 shows the horizontal wind speed (color scale) and direction (arrow) deduced from wind  
8 lidar and the sonic anemometer wind measurements near the ground. Back trajectories of the air  
9 masses ending in Mbour on 16 April 2015 at 2500 m (02:00 UTC, 06:00 UTC), at 900 m (00:00  
10 UTC) and at 700 m (06:00 UTC) are reported in Fig.3. These figures reveal complex  
11 stratification and dynamics of the lower troposphere on 15-16 April: we can distinguish four  
12 layers (A-D) from 100 m to a height of approximately 3000 m. In parallel, the wind field  
13 highlights the appearance of multi-layered wind structure mainly consisted of a northerly wind  
14 (downward arrow) prevailing near ground, which changes to an easterly wind (leftward arrow)  
15 with height (Fig. 2).

- 16 • Layer A, located between 1000 m to 3000 m (at 00:00 UTC), is associated with a small  
17 northerly wind speed ( $< 5$  m/s) in the lower part of the layer, and a slightly larger easterly  
18 wind speed ( $> 5$  m/s) above 2000 m. Layer A can be considered to be a continentalized  
19 maritime trade (CMT) wind which is one of oceanic origin that has been progressively  
20 altered by continental trade (CT), as follows from the back trajectories shown in Fig.3.  
21 Therefore, this layer is characterized by a mixture of maritime and continental air.
- 22 • Layer B located between 400 m - 800 m at the beginning of the study period rises  
23 progressively up to 700 m - 1000 m by the end of the dataset. This layer is characterized by  
24 northeasterly winds and high aerosol loading. According to the back trajectories shown in  
25 Fig. 3, this air mass was transported from a continental area (Mali) and was mainly advected  
26 by a southeasterly continental wind (CW).
- 27 • Layer C is a nocturnal low-level jet (LLJ). The jet core height is between 250 and 400 m  
28 with a maximum jet speed exceeding 15 m/s. The LLJ was observed throughout the night  
29 with a thickness that progressively increased with time perhaps being the causative  
30 mechanism for the corresponding increase in height of layer B (Fig.1). The LRCS values



1 within layer C decrease progressively up to the end of the observation period, perhaps due to  
2 dilution of the aerosol loading.

- 3 • Finally, layer D corresponds to the nocturnal boundary layer (NBL) characterized by high  
4 LRCS values and by small northerly or northwesterly wind speed ( $< 5$  m/s). The NBL top  
5 can be deduced from the LRCS profile discontinuity (Seibert et al., 2000) and is estimated as  
6 approximately 200-300 m during the night.

7 Fig.4 shows the particle extinction coefficient at 532nm (4-a), water vapor mixing ratio  
8 (4-b), lidar ratio (4-c) and depolarization ratio (4-d) both at 532 nm for the same time-height  
9 section as in Fig. 1 and 2. The water vapor can be used as a convenient tracer to separate dry  
10 continental air masses from oceanic air masses that are characterized by higher vapor content.  
11 Due to the geometrical overlap factor, the LILAS minimum height of the measurements shown  
12 in Fig. 4 is 800 m. Still, layer B (CW) is well observed starting at 03:00 UTC (Fig.4a) due to the  
13 increase of the layer height. The particle extinction coefficient  $\alpha_{532}$  in layer A increases after  
14 03:00 UTC while the mixing ratio is decreasing (Fig.4b). This may indicate that continental air  
15 mass advected by CT has become dominant. The lidar ratio  $LR_{532}$  of the particles associated with  
16 CT is about 55 sr while for CMT as observed during the first part of the observation period, it is  
17 lower (about 45 sr). The depolarization ratio  $\delta_{532}$  is about 30% in layer A and shows a small  
18 enhancement up to 35% for layer B. We should mention also, that for air masses which we  
19 consider as “continentalized maritime” the particle depolarization ratio is in excess of 25%,  
20 implying a significant amount of dust even in this layer.

21 To quantify vertical variations of water vapor mixing ratio and extinction coefficient  $\alpha_{532}$   
22 Fig.5 shows the corresponding vertical profiles averaged over the period 5:00-6:00 UTC . The  
23 WVMR in layer B containing dry continental air mass (at 1000 m) is approximately one-half of  
24 the values outside of the layer (at 1500 m). In layer A at 2800 m WVMR is approximately 1.5  
25 times higher compared to layer B, because layer A consists of a mixture of continental and  
26 oceanic air mass. These results demonstrate that water vapor, being a generally conserved  
27 quantity, is a helpful tracer for aiding the identification of air mass origin.

### 28

## 29 3. DUST PARTICLE PROPERTIES DERIVED FROM RAMAN LIDAR

### 30 OBSERVATIONS

#### 31 3.1. Day-to- day variation of particle intensive parameters

1 One of the goals of the SHADOW campaign was to study the dust particle intensive  
2 parameters such as extinction and backscattering Ångström exponents together with lidar and  
3 depolarization ratios. During March-April 2015 about 40 measurement sessions, including both  
4 day and night time periods, were performed. In the analysis presented below only night time  
5 measurements are considered, and for every session all lidar signals measured during the night  
6 are temporally averaged. Moreover, for an evaluation of day-to-day variations of the particle  
7 parameters we use only extinction and backscattering coefficients averaged within 1500 – 2000  
8 m height layer, where a high dust concentration is frequently observed. For such extensive  
9 averaging the uncertainties of derived parameters are mainly due to the systematical errors. Thus  
10 we estimate the uncertainty of extinction coefficient and lidar ratio calculation to be below 10%  
11 and 15% respectively for both wavelengths. Uncertainties of extinction and backscattering  
12 Ångström exponents derivation are estimated to be below  $\pm 0.2$ . It should be mentioned that only  
13 observations with particle depolarization great than 20% were selected to indicate a major dust  
14 contribution. The days with lower depolarization were characterized also by low particle  
15 extinction so we were not able to calculate intensive parameters with sufficient accuracy.

16 To give an overview of the variation in aerosol loading, the aerosol optical thickness  
17 (AOT) at 440 nm together with the extinction Ångström exponent (EAE)  $A_{380/500}^{\alpha}$  measured with  
18 Cimel sun photometer is reported in Fig.6 for the 10 March-23 April 2015 period. The AOT was  
19 relatively low (mainly below 0.4) for 17-28 March, but increased after 28 March reaching values  
20 up to 2.0. The high AOTs are associated with low values of the extinction Ångström exponent  
21 indicating numerous dust episodes (days with increased dust content). Fig.7 shows the particle  
22 extinction coefficient  $\alpha_{532}$  together with extinction (EAE) and backscattering (BAE) Ångström  
23 exponents  $A_{355/532}^{\alpha}$ ,  $A_{355/532}^{\beta}$  derived from the lidar measurements for the same time period.  
24 During 28 March – 15 April several strong dust episodes occurred as indicated by averaged over  
25 night values of extinction coefficient as high as  $0.5 \text{ km}^{-1}$ . For 85% of the considered cases, EAE  
26 is within the interval of  $-0.2 - 0.2$  while values of BAE are distributed over  $-0.55 - 0.5$  range,  
27 because BAE is more sensitive to the change of complex refractive index (CRI).

28 The day-to-day variation of the lidar ratios at 355 nm and 532 nm together with particle  
29 depolarization ratio at 532 nm is shown in Fig.8. The majority of the lidar ratios is contained  
30 within the range of 45-65 sr (96% and 82% for 532 nm and 355 nm, respectively) but for UV

1 about 10% of the cases are between 65 – 75 sr. The mean values of lidar ratios for both  
2 wavelengths are similar:  $LR_{355}=54\pm 8$  sr and  $LR_{532}=53\pm 8$  sr. The mean value of particle  
3 depolarization ratio is  $30\pm 4.5\%$ , however during the dust events depolarization ratio could  
4 increase up to  $35\pm 5\%$ .

#### 5 ***4.2. Vertical distribution of particle intensive properties***

6 The vertical distribution of particle intensive properties is strongly influenced by the  
7 origin of the air masses which during the SHADOW measurement period were coming either  
8 from ocean or continental regions. In this section, we present the results for three days (13, 29  
9 March and 10 April 2015) characterized by different types of air masses.

#### 10 ***13 March***

11 As follows from Fig.9, on 13 March at 21:00 UTC the air masses at the 3 heights (1500,  
12 2500 and 3500m) were transported mainly over the ocean, but the back trajectory at 1500 m  
13 presents a “loop” over continent, so the corresponding air masses may contain more dust  
14 compared to other heights. The relative humidity measured with meteorological sonde in Dakar  
15 was below 38% inside 1000 m – 2600 m height range and it increased up to 75% above 3350 m.  
16 Lidar measurements of water vapor mixing ratio are not available for this day. Fig.10 shows the  
17 vertical profiles of  $3\beta+2\alpha$  measurements together with lidar ratios  $LR_{355}$ ,  $LR_{532}$ , depolarization  
18 ratio  $\delta_{532}$ , and Ångström exponents  $A_{355/532}^{\alpha}$ ,  $A_{355/532}^{\beta}$  on 13 March 2015 averaged over the 20:30-  
19 21:30 time period. The aerosol layer extended up to 3500 m but the extinction coefficient  $\alpha$  was  
20 relatively small; at both 355 and 532 nm wavelengths  $\alpha$  did not exceed  $0.16 \text{ km}^{-1}$ . The particle  
21 depolarization ratio at 532 nm was approximately  $31\pm 4.5\%$  inside the dust layer (up to ~2750 m  
22 ) and decreased to less than 15% at 3250 m. Likewise, the  $A_{355/532}^{\alpha}$  and  $A_{355/532}^{\beta}$  are close to zero  
23 up to 2750 m, but start to increase above indicating the presence of smaller particles. The lidar  
24 ratios  $LR_{355}$  and  $LR_{532}$  are approximately  $53\pm 8$  sr inside the dust layer. Above 2750 m the values  
25 of LR are more noisy but do not seem to change.

#### 26 ***29 March***

27 The backtrajectories from the night of 29-30 March associated to a strong dust case are  
28 shown in Fig.11. The air masses at low altitude were transported over the continent and were  
29 strongly loaded with dust. The relative humidity was below 19% in 600 m – 1500 m height range  
30 Fig.12 presents the vertical profiles of the same particle parameters as in Fig.10 but for 29

1 March. Lidar measured water vapor mixing ratio shown in the same figure is below 2.5 g/kg.  
 2 The extinction coefficient  $\alpha$  inside the dust layer (below 1500 m) is greater than  $0.6 \text{ km}^{-1}$  for  
 3 both wavelengths. The backscattering coefficient  $\beta_{355 \text{ nm}}$  inside the dust layer is lower than  $\beta_{532}$   
 4 which is consistent with the lidar ratio larger at 355 nm than that at 532 nm with values as large  
 5 as 65 sr. The  $A_{355/532}^{\beta}$  (BAE) is negative and gets near -0.8, while EAE is still close to 0 as  
 6 observed on 13 March (Fig.10). The negative values of BAE can result from the spectral  
 7 dependence of the imaginary part of the dust refractive index (RI) which is larger at 355 than at  
 8 532 nm (e.g. Patterson et al., 1977; Müller et al., 2009; Ansmann et al., 2011).

9 The ground based measurements performed during the SAMUM campaign demonstrated  
 10 that the imaginary part of the dust RI could vary from  $m_i=0.005$  at 532 nm to  $m_i=0.02$  at 355 nm  
 11 (Ansmann, et al., 2011). Such a strong enhancement of  $m_i$  may lead to a decrease of the  
 12 backscattering coefficient (Veselovskii et al., 2010). To estimate the impact of the  $m_i$   
 13 enhancement at 355 nm on the values of EAE and BAE at 355/532 nm wavelengths, numerical  
 14 simulations were performed. Extinction and backscattering Ångström exponents were calculated  
 15 using the model of randomly oriented spheroids as described in (Veselovskii et al., 2010) for a  
 16 bimodal particle size distribution:

$$17 \quad \frac{dn(r)}{d \ln(r)} = \sum_{i=f,c} \frac{N_i}{(2\pi)^{1/2} \ln \sigma_i} \exp \left[ -\frac{(\ln r - \ln r_i)^2}{2(\ln \sigma_i)^2} \right]. \quad (1)$$

18 where  $N_{f,c}$  is particle number density in the fine ( $f$ ) and the coarse ( $c$ ) mode. Each mode is  
 19 represented by a lognormal distribution with modal radius  $r_{f,c}$  and dispersion  $\ln \sigma_{f,c}$ . For the  
 20 fine mode, values of  $r_f=0.1 \text{ }\mu\text{m}$  and  $\ln \sigma_f=0.4$  were used. For the coarse mode  $r_c=1.0 \text{ }\mu\text{m}$  and  
 21 three values  $\ln \sigma_c=0.4, 0.5, 0.6$  were considered. The three size distributions expressed in  
 22 volume are reported in the insert of Fig.13. The ratio  $N_c/N_f$  in all cases was 0.01, and the real part  
 23 of CRI was 1.55 for all wavelengths. The imaginary part was fixed at 0.005 for 532 nm while it  
 24 varied within the 0.005 – 0.05 range at 355 nm. Values of EAE and BAE as a function of  $m_i$  at  
 25 355 nm are given by Fig.13. The EAE shows no significant sensitivity to changes in  $m_i$ , but BAE  
 26 decreases rapidly as a function of  $m_i$  at 355 nm. The present sensitivity study is limited but  
 27 illustrates the importance of accounting for the right spectral dependence of  $m_i(\lambda)$ .

28 **10 April**

1           On April 10, the air masses were coming from continental regions and particle  
2 parameters showed large variation with height. We selected measurements during the period  
3 0:00-2:00 UTC for which the backward trajectories at 1:00 UTC are shown in Fig.14. The air  
4 masses at 2000 m and 3000 m originate from the dust-laden continental region (barren or  
5 sparsely vegetated areas), while at 4500 m the air masses come from regions covered by grass  
6 lands and savannas. Fig.15 shows profiles of the  $3\beta+2\alpha$  measurements together with particle  
7 intensive parameters. The particle extinction coefficient increases with height reaching a  
8 maximum value of around  $0.2 \text{ km}^{-1}$  for both wavelengths at a height of approximately 3000 m  
9 and then decreases up to 5 000m. The EAE is approximately zero up to 3000 m and then it  
10 increases to 1.0 at 4500 m. The BAE below 3000 m is smaller with minimum value  $A_{355/532}^{\beta} \approx -0.5$ ,  
11 but increase up to 4500 m where EAE and BAE are approximately equivalent. The  
12 depolarization ratio is around 30% in the 2000-3500 m range, and decreases for higher altitudes.  
13 The lidar ratio at 355 nm inside 2000-3500 m layer exceeds that at 532 nm (averaged values are  
14  $60 \pm 9$  sr and  $53 \pm 8$  sr correspondingly) and for higher altitudes the lidar ratios at both wavelengths  
15 are close. So we can identify different aerosol layers with different properties: mostly pure dust  
16 layer within the 2000-3500 m altitude range and mixed aerosols above it.

17           Fig.15 shows also the estimated profile of water vapor mixing ratio (WVMR) obtained  
18 from the lidar measurements. WVMR is less than 3 g/kg within the dust layer and increases  
19 above 3500 m reaching approximately 5.5 g/kg at 4000 m. There are clearly two distinct layers.  
20 If the derived properties of aerosols within the lower layer are representative of dust, the air mass  
21 above 4000m brings another particle type. Particles, characterized by lower depolarization ratio,  
22 are smaller since the EAE is increasing. Based on the analysis of the satellite data quick-looks  
23 (see for instance <http://earthobservatory.nasa.gov/GlobalMaps/>), the back-trajectories reporting  
24 in Fig. 14 show that the air mass at 4500m is coming from regions where fires were active during  
25 several days, which can result in emission of smoke particles transported over M'Bour few days  
26 later. The derived properties of aerosols within the 4000-5000m layer are consistent with this  
27 hypothesis.

28

## 29 **5. INVERSION OF RAMAN LIDAR OBSERVATIONS TO THE PARTICLE** 30 **MICROPHYSICS**

1           The lidar  $3\beta+2\alpha$  and  $3\beta+2\alpha+1\delta$  observations analyzed in the previous sections can be  
2 inverted into microphysical properties using regularization algorithm. As previously mentioned,  
3 in the case of irregularly shaped dust particles such inversion is more complicated compared to  
4 other aerosol types that may be well handled by spherical particle assumptions. In an earlier  
5 study, a model of randomly oriented spheroids for dust was used (Veselovskii et al., 2010). This  
6 model handles the dust particles as a mixture of spheres and spheroids, so an additional unknown  
7 parameter, spheroids volume fraction (SVF), appears. The SVF in principle can be determined in  
8 the process of inversion of  $3\beta+2\alpha+1\delta$  measurements thanks to the use of depolarization ratio as  
9 input parameter. However, for the dust layers, in a first guess, we assume a value of SVF=100%  
10 to decrease the number of retrieved parameters. The values of SVF>98% provided by  
11 AERONET for the days considered here support this assumption. In the process of inversion we  
12 used algorithm from (Veselovskii et al., 2010) and the “search space” parameters similar to those  
13 described in (Müller et al., 2013). The boundary of the inversion window has been set to  
14 minimum and maximum particle radii of 0.075 and 15  $\mu\text{m}$ , respectively. The real part of RI was  
15 allowed to vary in the range 1.35 - 1.65, while the imaginary part varied in the range 0 - 0.02.  
16 The refractive index was assumed to be spectrally independent. The effects of a possible spectral  
17 dependence of the imaginary part of RI will be considered at the end of this section.

18           Fig. 16 shows the particle volume density retrieved from  $3\beta+2\alpha$  measurements on 13  
19 March, 29 March and 10 April, which were discussed in the 4.2 section. The profiles of particle  
20 volume are given together with corresponding extinction coefficients at 532 nm. The volume –  
21 extinction ratio  $V/\alpha_{532}$  for these days is also reported. Inside the dust layer this ratio varies  
22 within the range  $(0.50-0.65)*10^{-6}$  m, while outside the dust layer, the  $V/\alpha_{532}$  ratio decreases. An  
23 overview of observed values of the volume – extinction ratio for dust, obtained from in situ,  
24 AERONET and lidar measurements is presented in Ansmann et al., 2012 and provides  $V/\alpha_{532}$   
25 varying within the range  $(0.60-1.29)*10^{-6}$  m. Thus our results are near the low boundary of these  
26 previously published results.

27           The profiles of the effective radius and the real part of RI are shown in Fig.17. The  
28 inverted effective radius inside the dust layer is between 1.05 and 1.25 $\mu\text{m}$  ( $1.15\pm 0.3 \mu\text{m}$ ) and  
29 similar for the 3 days. The AERONET retrievals provided column integrated values that are in  
30 the same range and agrees within the uncertainty. On 30 March early morning, when the dust

1 contribution to the AOT is prevailing, the effective radius  $r_{\text{eff}}=1.36 \mu\text{m}$  and it varies between  
2 0.918 and 1.70 depending on the days and time. The lidar retrievals indicate that the real part of  
3 the CRI in the dust layer varied from  $1.51\pm 0.05$  to  $1.57\pm 0.05$ , which is quite typical for desert  
4 dust (Patterson et al., 1977), while the AERONET retrievals yield values between approximately  
5 1.46 and 1.58 depending on the days. Outside of the dust layer the retrieval of  $m_R$  is not reliable  
6 because the assumption of  $\text{SVF}=100\%$  is not fulfilled and, as a result, the retrieved values of  $m_R$   
7 are overestimated (Veselovskii et al., 2010).

8 The values of the imaginary part of the CRI retrieved from lidar measurements are  
9 approximately 0.007 inside the dust layer. However, the retrieved value is associated to average  
10 value over spectral range and characterized by high uncertainty (Müller et al., 2013). Still, this  
11 uncertainty does not affect significantly the retrieved values of volume and effective radius  
12 (Veselovskii et al., 2013).

13 The regularization approach estimates also the particle volume size distribution (PSD),  
14 allowing to conclude, which of the modes (fine or coarse) is predominant. Fig.18 shows the  
15 PSDs derived from lidar measurements on 10 April for four height layers of 150 m width  
16 centered at 1940, 3150, 4070, 4370 m heights. For the layers with strong dust loadings (1940,  
17 3150 m) the coarse mode is dominant, at higher altitude outside the dust layer (4070, 4370 m),  
18 the fine mode (around  $0.15\mu\text{m}$ ) prevails. For comparison, the column integrated PSD obtained  
19 from AERONET level 1.5 data on 9 April at 18:00 UTC is also reported. The coarse mode looks  
20 shifted toward larger particles when compared to the lidar retrievals but the difference can be due  
21 to the spectral dependence of the imaginary part of  $m_I$ , as it will be discussed further in this  
22 section.

23 Depolarization measurements provide additional information about particle properties  
24 that can be used in the inversion algorithm as long as the forward model can compute the particle  
25 depolarization ratio with sufficient accuracy. Hereafter, we compare the retrieved aerosol  
26 parameters using  $3\beta+2\alpha$  or  $3\beta+2\alpha+1\delta$  observations. To perform such a comparison we calculated  
27 the ratio of the effective radii ( $R_s^r$ ) derived from  $3\beta+2\alpha+1\delta$  and  $3\beta+2\alpha$  data sets. Fig.19 shows  
28 the profiles of  $R_s^r$  for the same three days (the right part being associated with the bottom x-  
29 axis); a value of 1.0 would mean that the additional input has no impact on the retrieval. Inside  
30 the dust layer the ratio is about 1.15 for the measurements taken on 13 and 29 March. On 10

1 April, the ratio is noisier, but the average is still close to the results obtained for 13 and 29  
2 March. We should mention that the ratio of the particle volumes  $R_s^V$  is very close to  $R_s^r$ , so it is  
3 not shown in the figure. At present we are not able to make a definitive conclusion about which  
4 data set leads to a more accurate estimation of dust parameters. The dust parameters should be  
5 monitored independently for this kind of comparison. However, as mentioned in the  
6 Introduction, the spheroidal model has difficulty in reproducing high depolarization  
7 measurements. As a result, the inversion of  $3\beta+2\alpha+1\delta$  dust measurements provides the real part  
8 of RI about 1.45 and the imaginary part below 0.005, which is lower than expected values based  
9 on in situ measurements (Müller et al., 2013). So at present, in the case of pure dust we prefer to  
10 use  $3\beta+2\alpha$  measurements alone, because it leads to more realistic estimations of the refractive  
11 index. Still, the difference between the values retrieved from the two data sets is about 15%,  
12 which is lower than the uncertainty of the retrieval which we estimate to be of ~30% for both  
13 volume and radius. However, for mixtures of dust with other aerosols, depolarization  
14 measurements still should be used in inversion, otherwise the SVF can not be estimated  
15 correctly.

16 The inversion results presented in Fig.16, 17 are obtained assuming a spectrally  
17 independent refractive index while the imaginary part of CRI of dust is expected to increase in  
18 the UV spectral region. To test the effect of a spectrally dependent imaginary part  $m_I(\lambda)$  on the  
19 retrieval, we now assume that the imaginary parts at 1064 nm and 532 nm wavelengths are the  
20 same  $m_I(532) = m_I(1064)$ , while  $m_I(355) = 4m_I(532)$ . Such an enhancement of  $m_I$  at 355 nm is  
21 quite typical for Saharan dust (Ansmann et al., 2011). The  $3\beta+2\alpha$  measurements for the same  
22 three days are so inverted assuming this  $m_I(\lambda)$  spectral dependence as described in (Veselovskii  
23 et al., 2010), while the real part of the refractive index is assumed to be spectrally independent.  
24 Fig.19 (left part associated with top x-axis) shows profiles of  $R_{ml}^r$ , which is the ratio of the  
25 effective radii retrieved under the assumption of spectrally dependent and spectrally independent  
26 imaginary part of RI. Again, the corresponding ratios  $R_{ml}^V$  for the volumes are close to  $R_{ml}^r$  and we  
27 do not report them. As expected, the effect of  $m_I(\lambda)$  is more pronounced inside the dust layer,  
28 and on 29 March and 10 April (days characterized by negative BAE), the value of  $R_{ml}^r$  is up to  
29 1.5. Accounting for  $m_I(\lambda)$  dependence increases also the real part of RI, thus e on 29 March  $m_R$



1 increases from approximately 1.52 to 1.56 inside the dust layer. These model computations  
2 demonstrate that accounting for the spectral dependence of the imaginary part of RI in the dust  
3 layers may significantly increase the retrieved values of the effective radius and particle volume.  
4 In particular, it may explain smaller radii of the coarse mode particles retrieved from lidar  
5 measurements inside the dust layer (Fig.19) when compared to AERONET results. The effects of  
6 spectral dependence of  $m_I$  can be to some extent corrected by using  $m_I(\lambda)$  model based on in situ  
7 measurements and implying it in retrieval algorithm as described in (Veselovskii et al., 2010).

8

## 9 CONCLUSION

10 The lidar measurements performed in March-April 2015 during the first phase of the  
11 SHADOW campaign in Senegal has provided a significant amount of information about dust  
12 particle parameters. The use of rotational Raman scattering in the LILAS for 532 nm  
13 observations improved the  $\alpha_{532}$  measurements and, as a result, the calculation of lidar ratio and  
14 extinction Ångström exponent were improved as well. The mean values of lidar ratios of pure  
15 dust were about  $53 \pm 8$  sr for both 532 nm and 355 nm wavelengths, which agrees with the values  
16 observed during SAMUM 1 (Morocco) and SAMUM 2 (Cape Verde) campaigns. The mean  
17 value of particle depolarization ratio at 532 nm was  $30 \pm 4.5\%$ , however during strong dust  
18 episodes this ratio increased up to  $35 \pm 5\%$ , which is also in agreement with the results of  
19 SAMUM campaigns. The backscattering Ångström exponent at 355/532 nm wavelengths during  
20 the dust episodes decreased to  $\sim -0.7$ , while the EAE values, though being negative, were higher  
21 than  $-0.2$ . Low values of BAE may be a result of enhanced dust absorption at 355 nm, **which**  
22 **should depend on mineralogy at the location of dust origin.**

23 The inversion of  $3\beta+2\alpha$  measurements to particle microphysics in the case of dust is more  
24 challenging than other types of aerosols. The use of pure dust observations somewhat simplifies  
25 this task, because the contribution of the particles in the fine mode (which may have different  
26 origin) is insignificant. Moreover, in the retrieval of pure dust properties we don't need to  
27 consider the mixture of spheres and spheroids and can assume SVF=100%. The use of the  
28 spheroids model for the inversion of  $3\beta+2\alpha$  measurements leads to values of effective radius in  
29 reasonable agreement with AERONET observations and yields reasonable values of the real part  
30 of RI. However, the use of depolarization measurements ( $3\beta+2\alpha+1\delta$ ) in the inversion for pure

1 dust, which is characterized by a depolarization ratio  $\delta_{532}$  exceeding 30%, leads to values of  
2 effective radius and volume exceeding the corresponding values obtained from  $3\beta+2\alpha$   
3 measurements by a factor up to 1.15. At the same time, the values of  $m_R$  are decreased. These  
4 issues have already been discussed so at the current time we prefer to not use the depolarization  
5 ratio in the input data set for the inversion of dust particle parameters. We hope also that these  
6 discussions will stimulate development of the forward model accurately describing polarization  
7 properties of laser radiation backscattered by dust particles.

8         The analysis performed here demonstrates the importance of the spectral dependence of  
9 the imaginary part of RI in the UV spectral region. Model simulations demonstrate that including  
10  $m_I(\lambda)$  dependence may increase the values of effective radius and volume by a factor as large as  
11 1.5. Thus, at the moment, dust particle microphysical properties obtained by inversion of lidar  
12 measurements may contain significant biases. Further research is needed to develop techniques  
13 correcting these biases in order the uncertainty of the estimates of  $r_{\text{eff}}$  and  $V$  to remain below  
14 30%, which is a typical value when particles with prevailing fine mode are considered.

15         In addition to aerosol properties, the LILAS system provided profiles of the water vapor  
16 mixing ratio, which, being a conserved quantity, was frequently a convenient tracer that  
17 indicated the boundary between dry air masses transported over the continent and moist air  
18 masses transported over the ocean. The episodes considered in this paper were characterized  
19 mainly by low values of RH and the effects of the particles hygroscopic growth were not  
20 considered. Still, we have significant amount of the measurements in the condition of high RH,  
21 accompanied by formation of water and ice clouds near the dust layers. We plan to present these  
22 results in a separate publication.

23         During phase 1 of SHADOW the aerosols other than dust didn't occur in significant  
24 amount inside the height range available for the measurements, so this publication is focused  
25 mainly on the pure dust study. However in phase 2 the episodes of dust-smoke mixture were  
26 observed and such episodes provide opportunity to test the algorithm ability to profile the layers  
27 with different particle types. Such analysis is in progress and will be presented separately.

28  
29 **Acknowledgments:** The authors are very grateful to IRD-Dakar (Institut de Recherche pour le  
30 Développement) for their welcome and efficient support and also thank the labex CaPPA for  
31 supporting this campaign. The CaPPA project (Chemical and Physical Properties of the

1 Atmosphere) is funded by the French National Research Agency (ANR) through the PIA  
2 (Programme d'Investissement d'Avenir) under contract "ANR-11-LABX-0005-01" and by the  
3 Regional Council " Nord-Pas de Calais » and the "European Funds for Regional Economic  
4 Development (FEDER). Development of lidar retrieval algorithms was partly supported by  
5 Russian Science Foundation, (project No. 14-50-00034). The authors gratefully acknowledge the  
6 NOAA Air Resources Laboratory (ARL) for the provision of the HYSPLIT transport and  
7 dispersion model and/or READY website (<http://www.ready.noaa.gov>) used in this publication.

8

## 1 **References**

- 2 Ansmann, A. and Müller, D.: Lidar and atmospheric aerosol particles, in "Lidar. Range-Resolved  
3 Optical Remote Sensing of the Atmosphere", Weitkamp, C. ed., Springer, New York, 2005,  
4 pp. 105-141.
- 5 Ansmann, A., Petzold, A., Kandler, K., Tegen, I., Wendisch, M., Müller, D., Weinzierl, B.,  
6 Müller, T., Heintzenberg, J.: Saharan Mineral Dust Experiments SAMUM-1 and SAMUM-  
7 2: what have we learned?, *Tellus*, 63B, 403-429, 2011.
- 8 Ansmann, A., Seifert, P., Tesche, M., Wandinger, U.: Profiling of fine and coarse particle mass:  
9 case studies of Saharan dust and Eyjafjallajökull/Grimsvötn volcanic plumes. *Atmos. Chem.*  
10 *Phys.*, 12, 9399-9415, 2012.
- 11 Balkanski, Y., Schulz, M., Claquin, T., and Guibert, S.: Reevaluation of mineral aerosol radiative  
12 forcings suggests a better agreement with satellite and AERONET data, *Atmos. Chem. Phys.*,  
13 7, 81-95, 2007.
- 14 Biniotoglou, I., Basart, S., Alados-Arboledas, L., Amiridis, V., and co-authors: A methodology  
15 for investigating dust model performance using synergistic EARLINET/AERONET dust  
16 concentration retrievals. *Atmos. Meas. Tech.*, 8, 3577-3600, 2015.
- 17 Browning, K. A. and Wexler, R.: The determination of kinematic properties of a wind field using  
18 Doppler radar, *J. Appl. Meteor.*, 7, 105-113, 1968.
- 19 Burton, S. P., Vaughan, M. A., Ferrare, R. A. and Hostetler, C. A.: Separating mixtures of  
20 aerosol types in airborne High Spectral Resolution Lidar data. *Atmos. Meas. Tech.*, 7, 419-  
21 436, 2014.
- 22 De Tomasi, F., Blanco, A., and Perrone, M. R.: Raman lidar monitoring of extinction and  
23 backscattering of African dust layers and dust characterization. *Appl. Opt.* 42, 1699-1709,  
24 2003.
- 25 Di Girolamo, P., Summa, D., Bhawar, R., Di Iorio, T., Cacciani, M., Veselovskii, I., Dubovik,  
26 O., Kolgotin, A.: Raman lidar observations of a Saharan dust outbreak event:  
27 characterization of the dust optical properties and determination of particle size and  
28 microphysical parameters, *Atmospheric Environment*. 50, 66-78, 2012.
- 29 Dubovik, O., Sinyuk, A., Lapyonok, T., Holben, B.N., Mishchenko, M., Yang, P., Eck, T.F.,  
30 Volten, H., Munoz, O., Veihelmann, B., van der Zande, W.J., Leon, J.-F., Sorokin, M.,  
31 Slutsker, I.: Application of spheroid models to account for aerosol particle nonsphericity in

1 remote sensing of desert dust, *J. Geophys. Res.*, 111, D11208, doi:10.1029/2005JD006619,  
2 2006.

3 Esselborn, M., Wirth, M., Fix, A., Weinzierl, B., Rasp, K., Tesche, M., and Petzold, A.: Spatial  
4 distribution and optical properties of Saharan dust observed by airborne high spectral  
5 resolution lidar during SAMUM 2006, *Tellus B*, 61, 131–143, 2009.

6 Formenti, P., Schütz, L., Balkanski, Y., Desboeufs, K., Ebert, M., Kandler, K., Petzold, A.,  
7 Scheuvens, D., Weinbruch, S., and Zhang, D.: Recent progress in understanding physical and  
8 chemical properties of African and Asian mineral dust, *Atmos. Chem. Phys.*, 11, 8231-8256,  
9 doi:10.5194/acp-11-8231-2011, 2011.

10 Formenti P., A. Klaver, S. Chevaillier, E. Journet, J. Rajot, Mapping the physico-chemical  
11 properties of mineral dust in western Africa: mineralogical composition, *Atmos. Chem. Phys.*,  
12 14, 10663-1068, 2014.

13 Freudenthaler, V., Esselborn, M., Wiegner, M., Heese, B., Tesche, M. and co-authors:  
14 Depolarization ratio profiling at several wavelengths in pure Saharan dust during SAMUM  
15 2006, *Tellus* 61B, 165–179, 2009.

16 Gasteiger, J., Wiegner, M., Groß, S., Freudenthaler, V., Toledano, C., Tesche, M., and Kandler,  
17 K.: Modeling lidar-relevant optical properties of complex mineral dust aerosols, *Tellus B*,  
18 63, 725-741, 2011.

19 Kandler, K., Lieke, K., Benker, N., Emmel, C., Küpper, M., Müller-Ebert, D., Ebert, M.,  
20 Scheuvens, D., Schladitz, A., Schütz, L., Weinbruch, S.: Electron microscopy of particles  
21 collected at Praia, Cape Verde, during the Saharan Mineral Dust Experiment: Particle  
22 chemistry, shape, mixing state and complex refractive index. *Tellus* 63B, 475-496, 2011.

23 Klett J.D., “Lidar inversion with variable backscatter/extinction ratios”, *Appl. Opt.* 24, 1638-  
24 1643, 1985.

25 Kumer, V.-M., Reuder, J., Furevik, B.R.: A comparison of LiDAR and radiosonde wind  
26 measurements, *Energy Procedia*, 53, 214-220, 2014.

27 Li, W. J., and Shao, L. Y.: Observation of nitrate coatings on atmospheric mineral dust particles  
28 *Atmos. Chem. Phys.*, 9, 1863–1871, 2009.

29 Mahowald, N. M., Kloster, S., Engelstaedter, S., Moore, J. K., Mukhopadhyay, S., McConnell, J.  
30 R., Albani, S., Doney, S. C., Bhattacharya, A., Curran, M. A. J., Flanner, M. G., Hoffman, F.  
31 M., Lawrence, D. M., Lindsay, K., Mayewski, P. A., Neff, J., Rothenberg, D., Thomas, E.,

1 Thornton, P. E., and Zender, C. S.: Observed 20th century desert dust variability: impact on  
2 climate and biogeochemistry, *Atmos.Chem. Phys.*, 10, 10875-10893, 2010.

3 McConnell, C. L., Highwood, E. J., Coe, H., Formenti, P., Anderson, Osborne, B. S., Nava, S.,  
4 Desboeufs, K., Chen, G., Harrison, M. A. J.: Seasonal variations of the physical and optical  
5 characteristics of Saharan dust: results from the Dust Outflow and Deposition to the Ocean  
6 (DODO) experiment, *J. Geophys. Res.* **113**, D14S05, doi:10.1029/2007JD009606, 2008.

7 Mishchenko, M.I., L.D. Travis, R.A. Kahn, and R.A. West, Modeling phase functions for  
8 dustlike tropospheric aerosols using a mixture of randomly oriented polydisperse spheroids,  
9 *J. Geophys. Res.*, Vol. 102, 16831-16847, 1997

10 Mona, L., Amodeo, A., Pandolfi, M., Pappalardo, G.: Saharan dust intrusions in the  
11 Mediterranean area: three years of Raman lidar measurements. *J. Geophys. Res.*, 111,  
12 D16203, doi:10.1029/2005JD006569, 2006.

13 Müller, T., Schladitz, A., Massling, A., Kaaden, N., Kandler, K. and Wiedensohler A.: Spectral  
14 absorption coefficients and imaginary parts of refractive indices of Saharan dust during  
15 SAMUM-1, *Tellus 61B*, 79–95, 2009.

16 Müller, D., Wandinger, U., and Ansmann, A.: Microphysical particle parameters from extinction  
17 and backscatter lidar data by inversion with regularization: theory, *Appl. Opt.* 38, 2346-2357,  
18 1999.

19 Müller, D., Mattis, I., Wandinger, U., Ansmann, A., Althausen, D., Stohl, A.: Raman lidar  
20 observations of aged Siberian and Canadian forest fire smoke in the free troposphere over  
21 Germany in 2003: Microphysical particle characterization, *J. Geophys. Res.*, 110, D17201,  
22 doi:10.1029/2004JD005756, 2005.

23 Müller, D., Weinzierl, B., Petzold, A., Kandler, K., Ansmann, A., Müller, T., Tesche, M.,  
24 Freudenthaler, V., Esselborn, M., Heese, B., Althausen, D., Schladitz, A., Otto, S., and  
25 Knippertz, P.: Mineral dust observed with AERONET Sun photometer, Raman lidar and in  
26 situ instruments during SAMUM 2006: shape-independent particle properties, *J. Geophys.*  
27 *Res.*, 115, D11207, doi:10.1029/2009JD012523, 2010.

28 Müller, D., Veselovskii, I., Kolgotin, A., Tesche, M., Ansmann, A., Dubovik, O.: Vertical  
29 profiles of pure dust (SAMUM-1) and mixed smoke-dust plumes (SAMUM-2) inferred from  
30 inversion of multiwavelength Raman/polarization lidar data and comparison to AERONET  
31 retrievals and in-situ observations, *Appl.Opt.* 52, 3178-3202, 2013.

1 Nisantzi, A., Mamouri, R. E., Ansmann, A., Schuster, G. L., Hadjimitsis, D. G.: Middle East  
2 versus Saharan dust extinction-to-backscatter ratios. *Atmos. Chem. Phys.*, 15, 7071–7084,  
3 2015.

4 Papayannis, A., Amiridis, V., Mona, L., Tsaknakis, G., Balis, D., Bösenberg, J., Chaikovski, A.,  
5 De Tomasi, F., Grigorov, I., Mattis, I., Mitev, V., Müller, D., Nickovic, S., Pérez, C.,  
6 Pietruczuk, A., Pisani, G., Ravetta, F., Rizi, V., Sicard, M., Trickl, T., Wiegner, M.,  
7 Gerding, M., Mamouri, R. E., D’Amico, G., and Pappalardo, G.: Systematic lidar  
8 observations of Saharan dust over Europe in the frame of EARLINET (2000–2002), *J.*  
9 *Geophys. Res.*, 113, D10204, doi:10.1029/2007JD009028, 2008.

10 Papayannis, A., Mamouri, R. E., Amiridis, V., Remoundaki, E., Tsaknakis, G., Kokkalis, P.,  
11 Veselovskii, I., Kolgotin, A., Nenes, A., and Fountoukis, C.: Optical-microphysical  
12 properties of Saharan dust aerosols and composition relationship using a multi-wavelength  
13 Raman lidar, in situ sensors and modelling: a case study analysis, *Atmos. Chem. Phys.* 12,  
14 4011-4032 (2012).

15 Patterson, E.M., Gillette, D.A., Stockton, B.H.: Complex Index of Refraction Between 300 and  
16 700 nm for Saharan Aerosols, *J. Geophys. Res.* 82, 3153 - 3160, 1977.

17 Redelsperger, J.-L., Thorncroft, C. D., Diedhiou, A., Lebel, T., Parker, D. J., Polcher, J.: African  
18 Monsoon Multidisciplinary Analysis: an international research project and field campaign.  
19 *Bull. Am.Meteorol. Soc.* 87, 1739–1746, 2006.

20 Reid, J. S. and Maring, H. B: Foreword to special section on the Puerto Rico Dust Experiment  
21 (PRIDE), *J. Geophys. Res.* 108, 8585, doi:10.1029/2003JD003510, 2003.

22 Ruchith, R.D. and Ernest Raj, P.: Features of nocturnal low level jet (NLLJ) observed over a  
23 tropical Indian station using high resolution Doppler wind lidar, *Journal of Atmospheric and*  
24 *Solar-Terrestrial Physics*, 123, 113-123, 2015.

25 Sakai, T., Nagai, T., Nakazato, M., Mano, Y., and Matsumura, T: Ice clouds and Asian dust studied  
26 with lidar measurements of particle extinction-to-backscatter ratio, particle depolarization,  
27 and water-vapor mixing ratio over Tsukuba. *Appl.Opt.* 42, 7103-7116, 2003.

28 Schwanghart, W. and Schütt, B.: Meteorological causes of Harmattan dust in West Africa,  
29 *Geomorphology*, 95, 412-428, 2008.

1 Seibert, P., Beyrich, F., Gryning S., Joffre, S., Rasmussen, A., Tercier, P.: Review and  
2 intercomparison of operational methods for the determination of the mixing height,  
3 *Atmospheric Environment*, 34, 1001–1027, 2000.

4 Shimizu, A., Sugimoto, N., Matsui, I., Arao, K., Uno, I., Murayama, T., Kagawa, N., Aoki, K.,  
5 Uchiyama, A., Yamazaki, A.: Continuous observations of Asian dust and other aerosols by  
6 polarization lidars in China and Japan during ACE-Asia, *J. Geophys. Res.*, 109, D19S17,  
7 doi:10.1029/2002JD003253, 2004.

8 Sokolik, I. N. and Toon, O. B.: Direct radiative forcing by anthropogenic airborne mineral  
9 aerosols, *Nature*, 381, 681–683, 1996.

10 Stein, A.F., Draxler, R.R, Rolph, G.D., Stunder, B.J.B., Cohen, M.D., and Ngan, F.: NOAA's  
11 HYSPLIT atmospheric transport and dispersion modeling system, *Bull. Amer. Meteor. Soc.*,  
12 96, 2059-2077, 2015.

13 Tanre, D., Haywood, J., Pelon, J., Leon, J.-F., Chatenet, B., Formenti, P., Francis, P., Goloub, P.,  
14 Highwood, E. J., Myhre, G.: Measurements and modeling of the Saharan dust radiative  
15 impact: overview of the Saharan Dust Experiment (SHADE). *J. Geophys. Res.* 108, 8574,  
16 doi:10.1029/2002JD003273, 2003.

17 Tesche, M., Ansmann, A., Müller, D., Althausen, D., Engelmann, R., Freudenthaler, V., and  
18 Groß, S.: Vertically resolved separation of dust and smoke over Cape Verde using  
19 multiwavelength Raman and polarization lidars during Saharan Mineral Dust Experiment  
20 2008, *J. Geophys. Res.*, 114, D13202, doi:10.1029/2009JD011862, 2009a.

21 Tesche, M., Ansmann, A., Müller, D., Althausen, D., Mattis, I., Heese, B., Freudenthaler, V.,  
22 Wiegner, M., Eseelborn, M., Pisani, G., and Knippertz, P.: Vertical profiling of Saharan dust  
23 with Raman lidars and airborne HSRL in southern Morocco during SAMUM, *Tellus B*, 61,  
24 144–164, doi:10.1111/j.1600-0889.2008.00390.x, 2009b.

25 Tesche, M., Groß, S., Ansmann, A., Müller, D., Althausen, D., Freudenthaler, V., and Esselborn,  
26 M.: Profiling of Saharan dust and biomass-burning smoke with multiwavelength  
27 polarization Raman lidar at Cape Verde, *Tellus B*, 63, 649–676, doi:10.1111/j.1600-  
28 0889.2011.00548.x, 2011.

29 Thobois, L. and Soderholm, J.: Observing clear air close proximity environment of severe  
30 storms, *Meteorological Technology International*, 9, 132-135, 2015.



1 Veselovskii I., Kolgotin, A., Griaznov, V., Müller, D., Wandinger, U., Whiteman, D.:  
2 Inversion with regularization for the retrieval of tropospheric aerosol parameters from multi-  
3 wavelength lidar sounding, *Appl.Opt.* 41, 3685-3699, 2002.

4 Veselovskii I., O. Dubovik, A. Kolgotin, T. Lapyonok, P. Di Girolamo, D. Summa, D. N.  
5 Whiteman, M. Mishchenko, and D. Tanré, 2010: Application Of Randomly Oriented  
6 Spheroids For Retrieval Of Dust Particle Parameters From Multiwavelength Lidar  
7 Measurements, *J. Geophys. Res.*, **115**, D21203, doi:10.1029/2010JD014139, 2010.

8 Veselovskii I., D. N. Whiteman, M. Korenskiy, A. Kolgotin, O. Dubovik, D. Perez-Ramirez, A.  
9 Suvorina.: Retrieval of spatio-temporal distributions of particle parameters from multi-  
10 wavelength lidar measurements using the linear estimation technique and comparison with  
11 AERONET, *Atmos. Meas. Tech.* 6, 2671-2682, 2013.

12 Veselovskii, I., Whiteman, D. N., Korenskiy, M., Suvorina, A., Kolgotin, A., Lyapustin, A.,  
13 Wang, Y., Chin, M., Bian, H. Kucsera, T. L., Perez-Ramirez, D., Holben, B.:  
14 Characterization of forest fire smoke event near Washington, D.C. in Summer 2013 with  
15 multi-wavelength lidar. *Atmos. Chem. Phys.* 15, 1647–1660, 2015.

16 Veselovskii, I., Whiteman, D. N., Korenskiy, M., Suvorina, A., Perez-Ramirez, D.: Use of  
17 rotational Raman measurements in multiwavelength aerosol lidar for evaluation of particle  
18 backscattering and extinction, *Atmos. Meas. Tech.*, 8, 4111–4122, 2015.

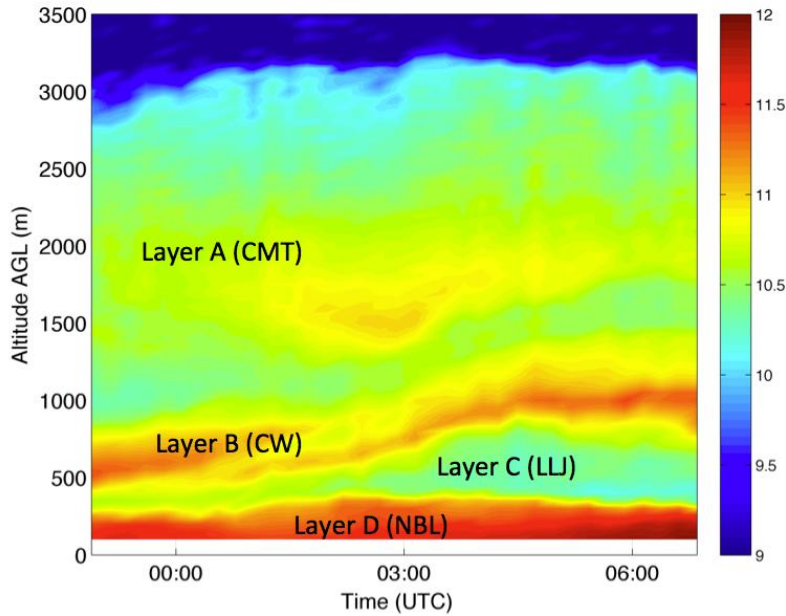
19 Wagner, J., Ansmann, A., Wandinger, U., Seifert, P., Schwarz, A., Tesche, M., Chaikovsky, A.,  
20 Dubovik, O.: Evaluation of the Lidar/Radiometer Inversion Code (LIRIC) to determine  
21 microphysical properties of volcanic and desert dust, *Atmos. Meas. Tech.*, 6, 1707–1724,  
22 2013.

23 Whiteman, D., Melfi, S., Ferrare, R.: Raman lidar system for measurement of water vapor and  
24 aerosols in the Earth's atmosphere", *Appl. Opt.* 31, 3068-3082, 1992.

25 Wiegner, M., Gasteiger, J., Kandler, K., Weinzierl, B., Rasp, K., Esselborn, M., Freudenthaler,  
26 V., Heese, B., Toledano, C., Tesche, M., Althausen, D.: Numerical simulations of optical  
27 properties of Saharan dust aerosols with emphasis on lidar applications. *Tellus* 61B, 180–  
28 194, 2009.

29 Xie, C., Nishizawa,T., Sugimoto,N., Matsui,I., and Wang,Z.: Characteristics of aerosol optical  
30 properties in pollution and Asian dust episodes over Beijing, China. *Appl.Opt.* 47, 4945-  
31 4951, 2008.

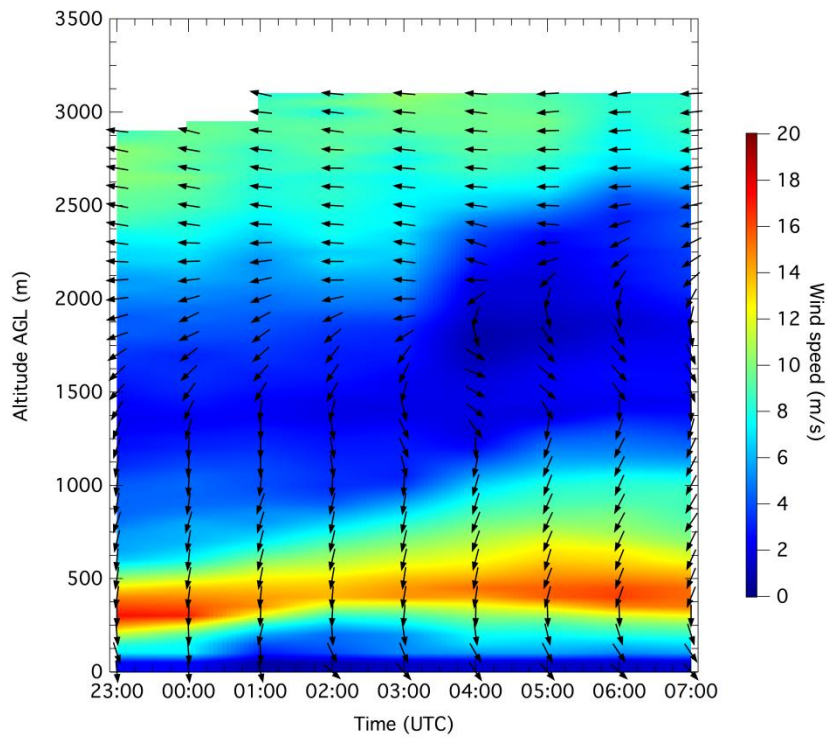
1  
2  
3  
4



5  
6  
7  
8  
9  
10  
11

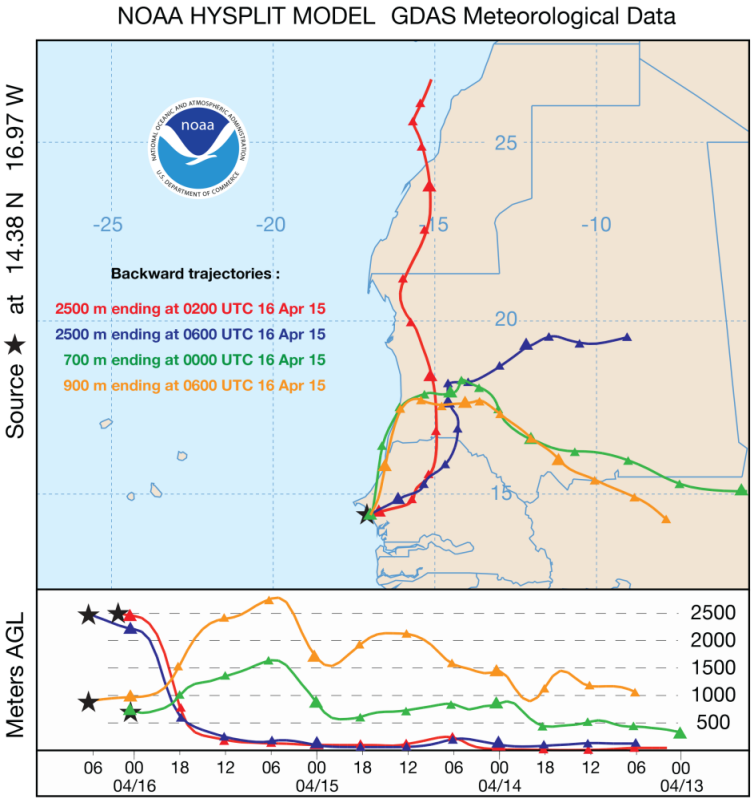
Fig.1. Time-height section of the logarithmic range corrected lidar signal (in arbitrary units) deduced from the Doppler lidar measurements during the 15-16 April 2015 night at Mbour. The stratification is represented by four layers: (A) continentalized maritime trade (CMT), (B) Layer advected mainly by a continental wind (CW), (C) low-level jet (LLJ) and (D) nocturnal boundary layer (NBL).

1



2  
3

4 Fig. 2. Time-height section of horizontal wind direction (arrows) and wind speed (color map)  
5 deduced from Doppler lidar during 15-16 April. Leftward and downward arrows represent,  
6 respectively, easterly wind and northerly wind



1

2 Fig.3. Back trajectories of the air masses ending in Mbour on 16 April 2015 at 2500 m (02:00

3 UTC, 06:00 UTC), at 700 m (00:00 UTC) and at 900 m (06:00 UTC). First two back trajectories

4 correspond layer A from Fig.1, while last two back trajectories correspond layer B from the same

5 figure.

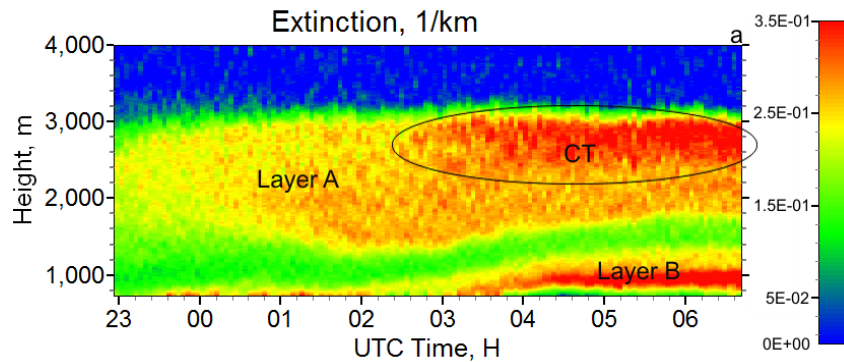
6

7

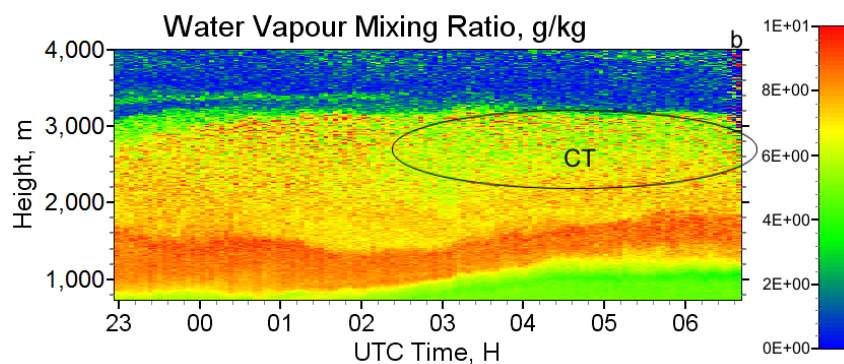
8

9

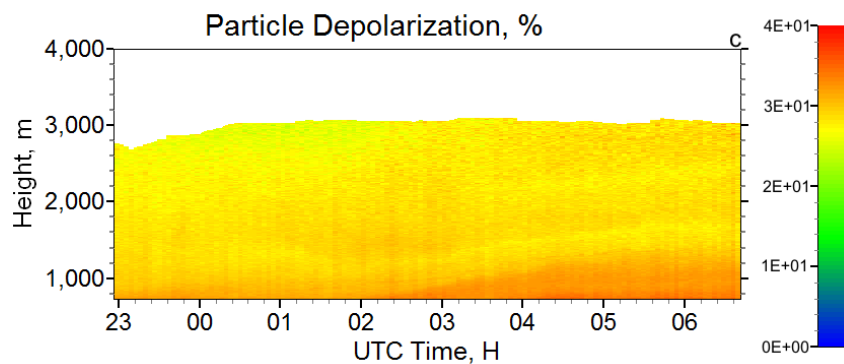
10



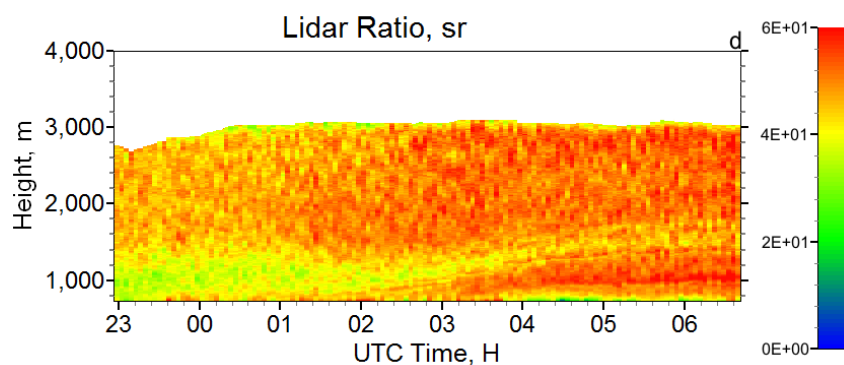
1



2

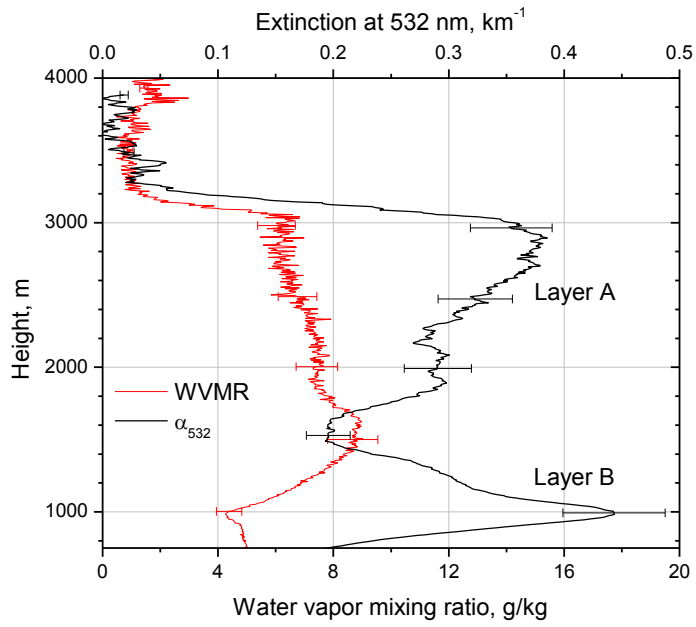


3



4

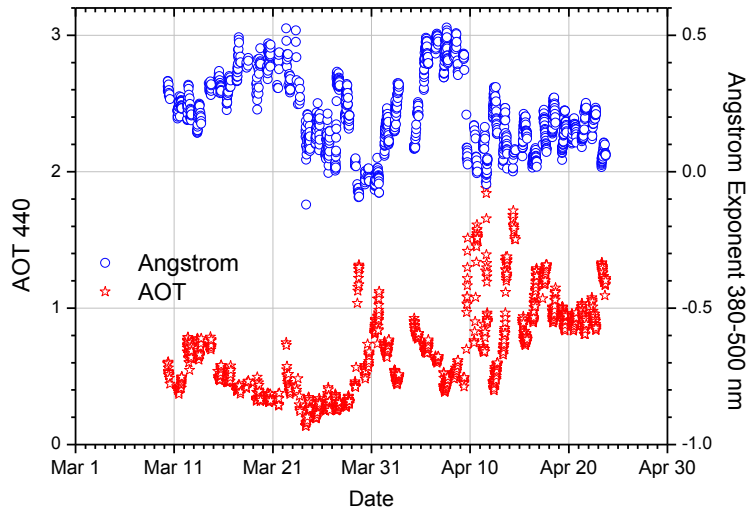
5 Fig.4. Height-temporal distribution of particle characteristics: (a) extinction coefficient  $\alpha_{532}$ , (b)  
 6 water vapor mixing ratio, (c) particle depolarization and (d) lidar ratio  $LR_{532}$  measured during the  
 7 15-16 April 2015 night.



1  
 2 Fig.5. Vertical profiles of particle extinction coefficient at 532 nm and water vapor mixing ratio  
 3 on 16 April 2015. Results are averaged over 5:00-6:00 UTC temporal interval.

4  
 5  
 6

1



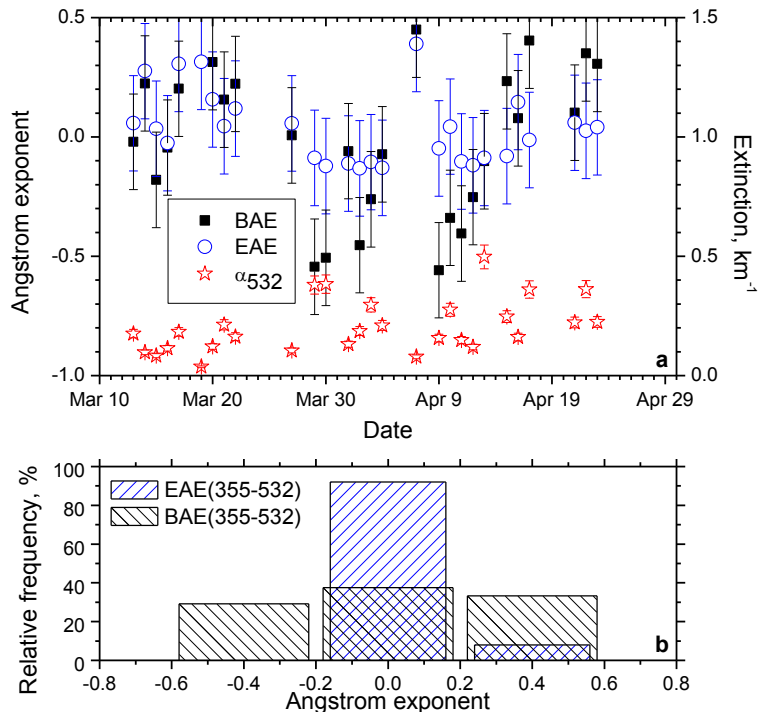
2

3 Fig.6. Aerosol optical thickness (AOT) at 440 nm and the extinction Ångström exponent at 380-  
4 550 nm wavelengths provided by AERONET in Mbour for March – April 2015 period.

5

6

1



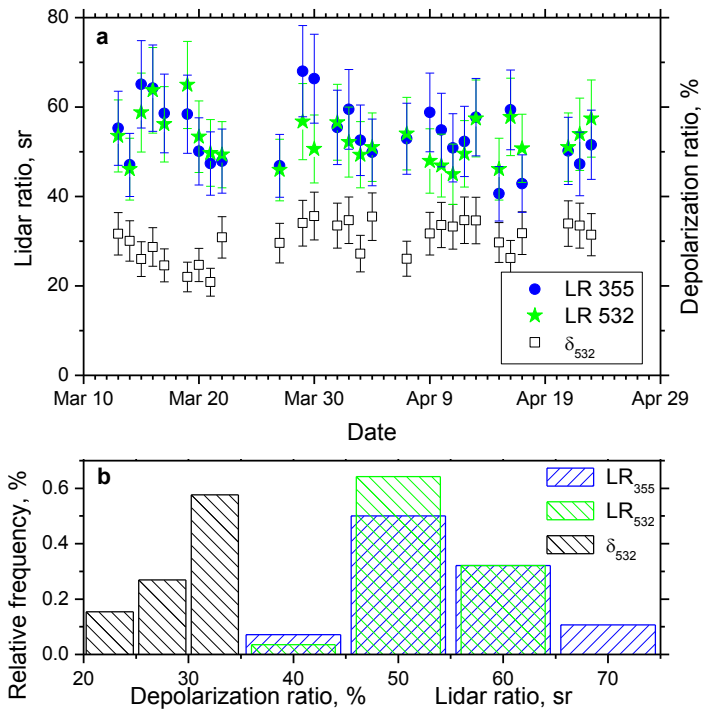
2

3 Fig. 7. (a) Particle extinction coefficient at 532 nm together with backscattering and extinction  
4 Ångström exponents at 355/532 nm, derived from lidar measurements within 1500 m – 2000 m  
5 layer for period March-April 2015. (b) Frequency distributions of BAE and EAE.

6



1

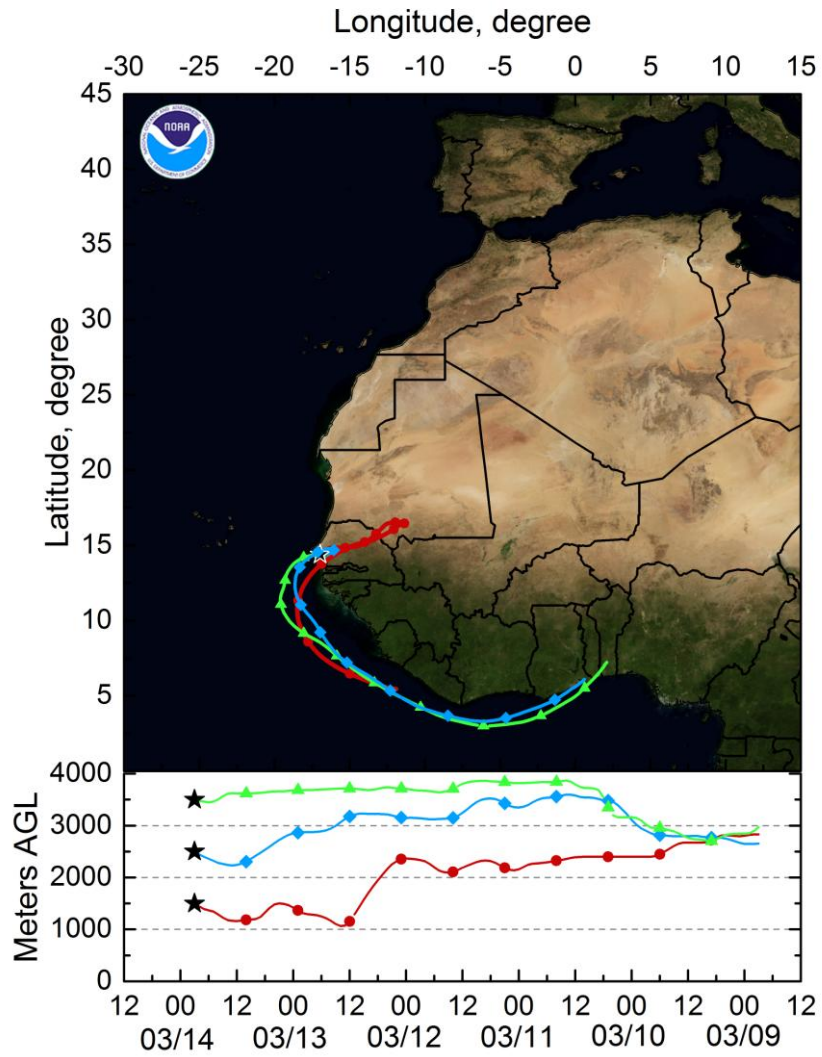


2

3 Fig. 8. (a) Lidar ratios at 355 nm and 532 nm together with particle depolarization ratios at 532  
4 nm derived from lidar measurements within 1500 m – 2000 m layer for period March-April  
5 2015. (b) Frequency distribution of lidar and depolarization ratios.

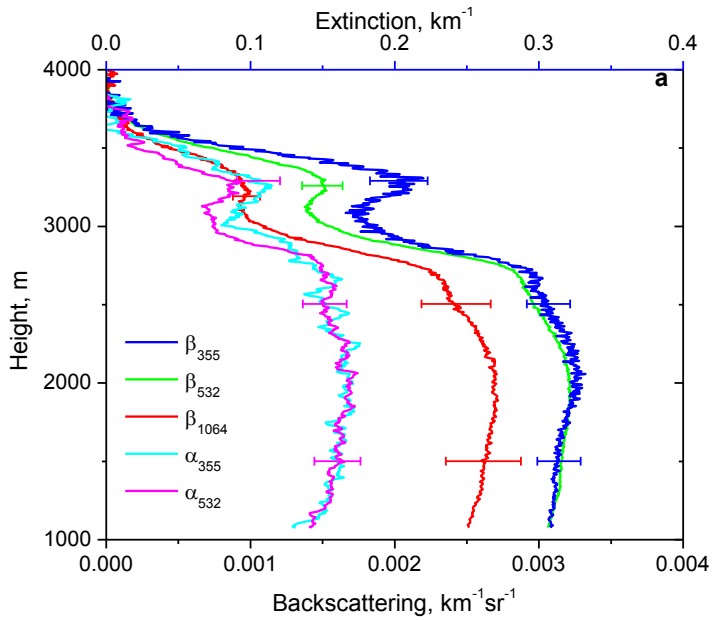
6

7

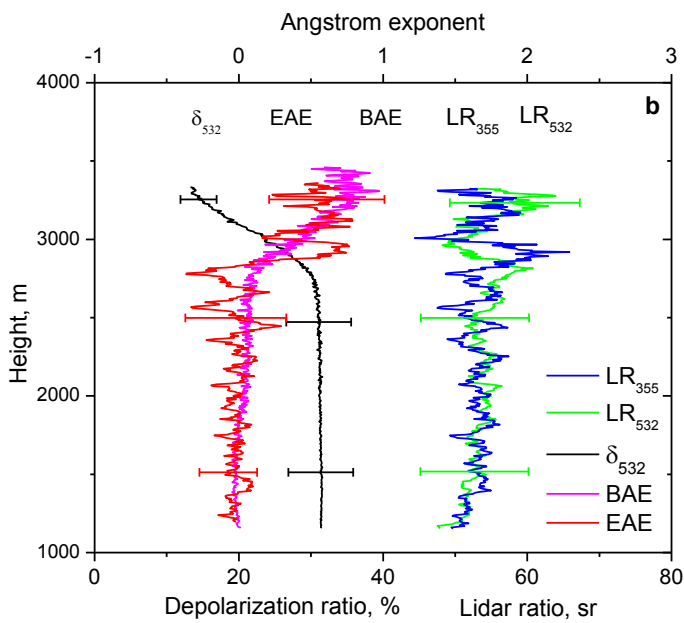


1  
2  
3  
4  
5  
6  
7  
8  
9

Fig.9. Five-day backward trajectories for the air mass in Mbour at altitudes 1500 m, 2500 m, 3500 m, on 13 March 2015 at 21:00 UTC.



1

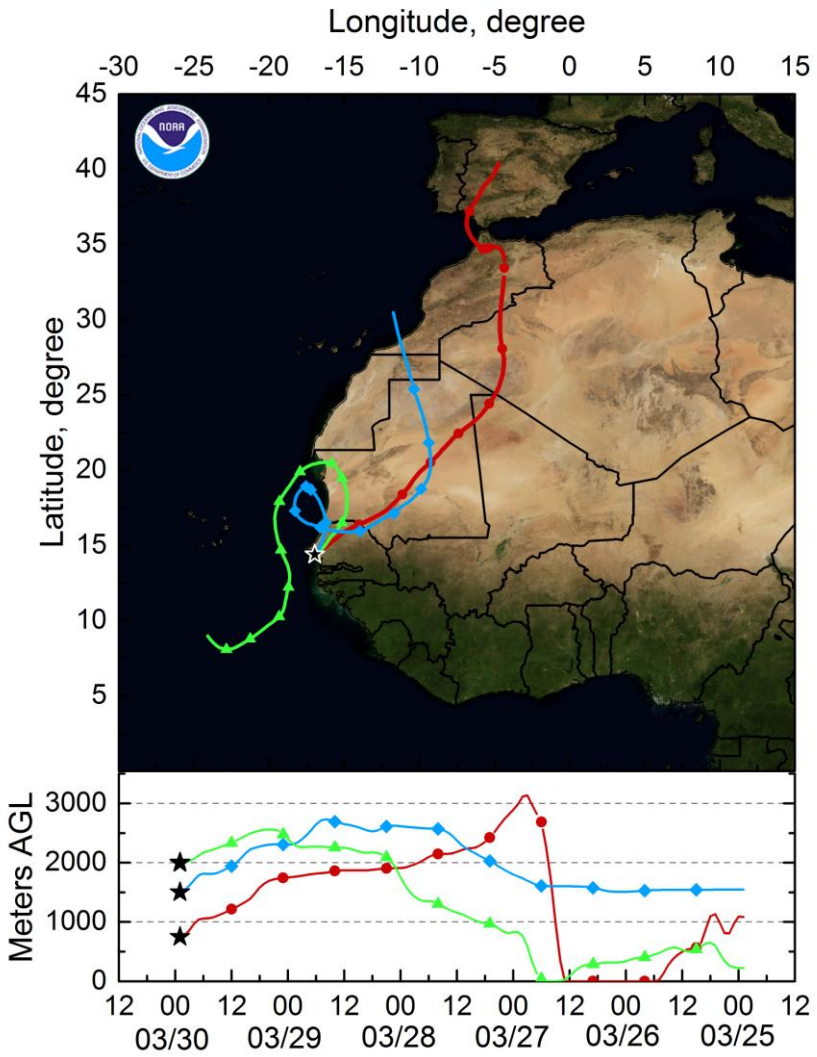


2

3 Fig.10. Vertical profiles of (a) backscattering and extinction coefficients and (b) lidar ratios,  
 4 depolarization ratio, backscattering and extinction Ångström exponents at 355/532 nm measured  
 5 on 13 March 2015 for period 20:30-21:30 UTC.

6

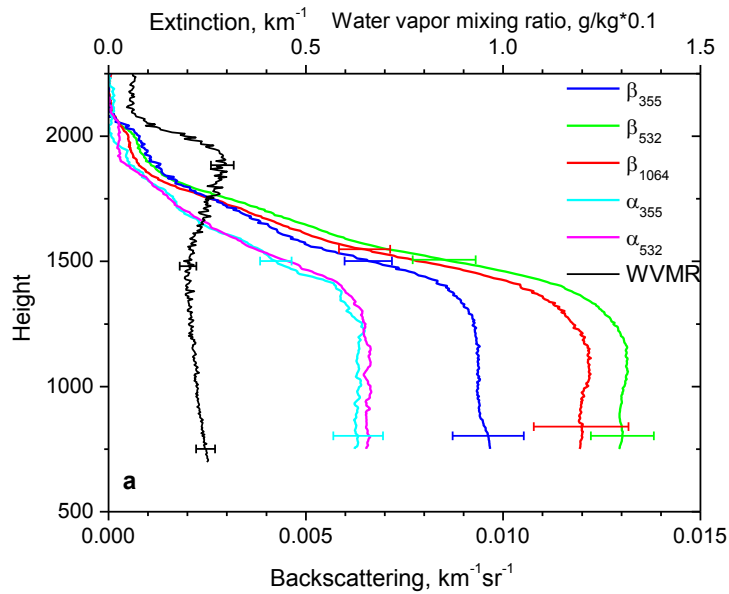
7



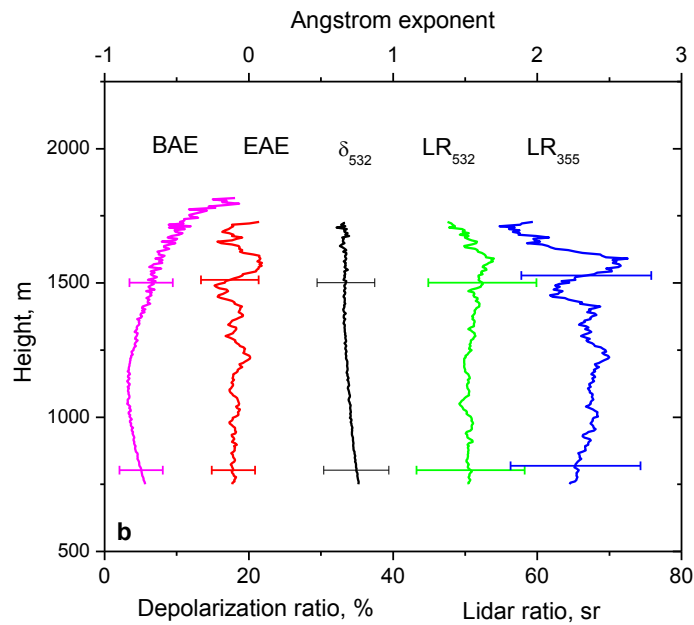
1  
2  
3  
4  
5

Fig.11. Five-day backward trajectories for the air mass in Mbour at altitudes 750 m, 1500 m, 2000 m on 29 March 2015 at 23:00 UTC.

1



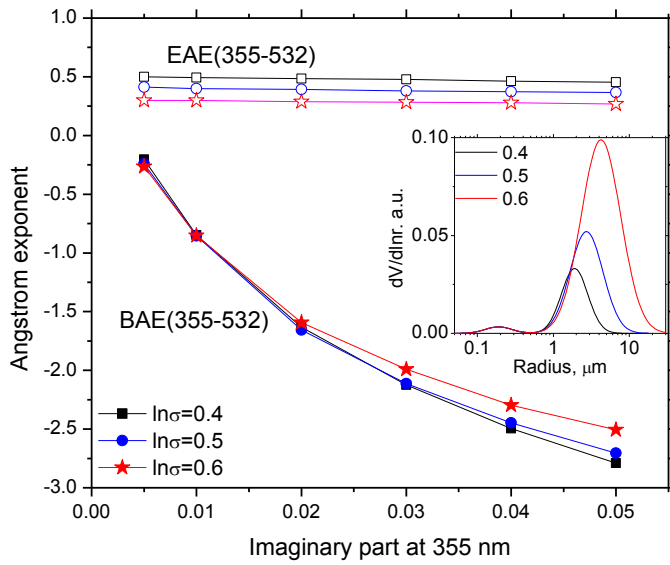
2



3

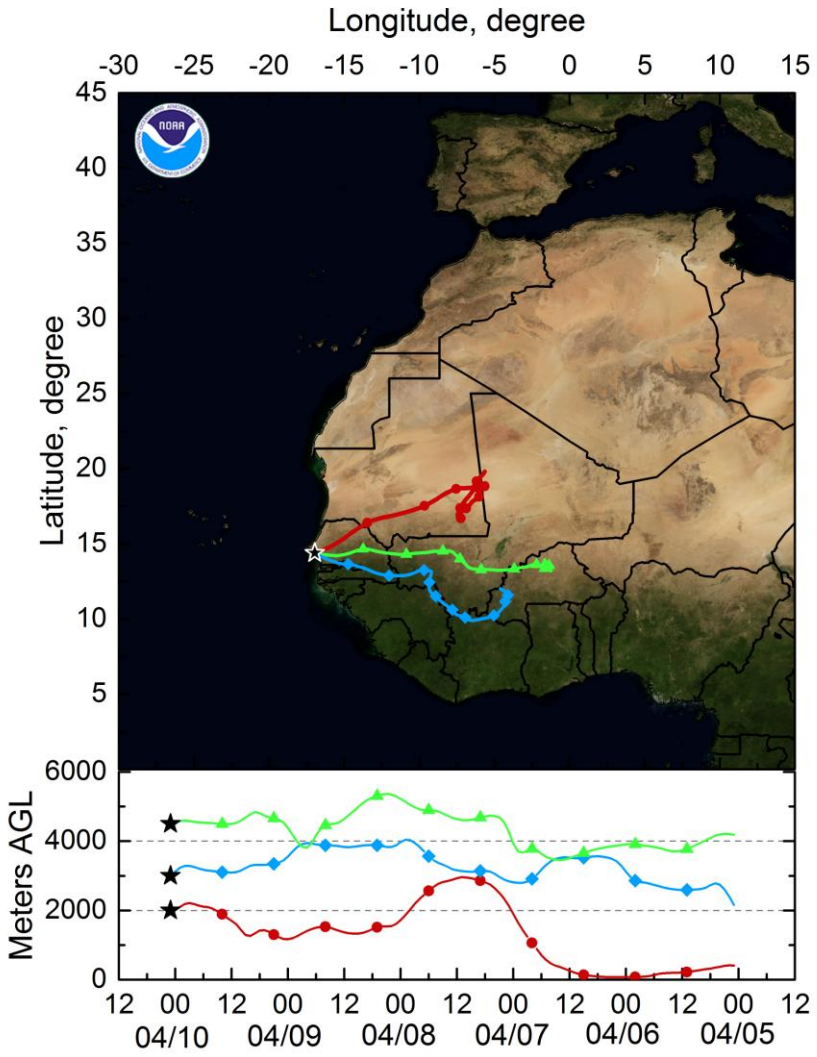
4 Fig.12. Vertical profiles of (a) backscattering and extinction coefficients and (b) lidar ratios,  
5 depolarization ratio, backscattering and extinction Ångström exponents at 355/532 nm measured  
6 on 29 March 2015 for period 22:00-23:30 UTC.

7



1  
 2 Fig.13. Extinction and backscattering Ångström exponent for 355/532nm wavelengths as a  
 3 function of the imaginary part of the refractive index at 355 nm. The CRI at 532 nm was kept  
 4  $m=1.55-i.005$ . Computations were performed using the model of randomly oriented spheroids.  
 5 The insert shows three bimodal PSDs with  $\ln\sigma=0.4, 0.5, 0.6$  used in computations.  
 6

1



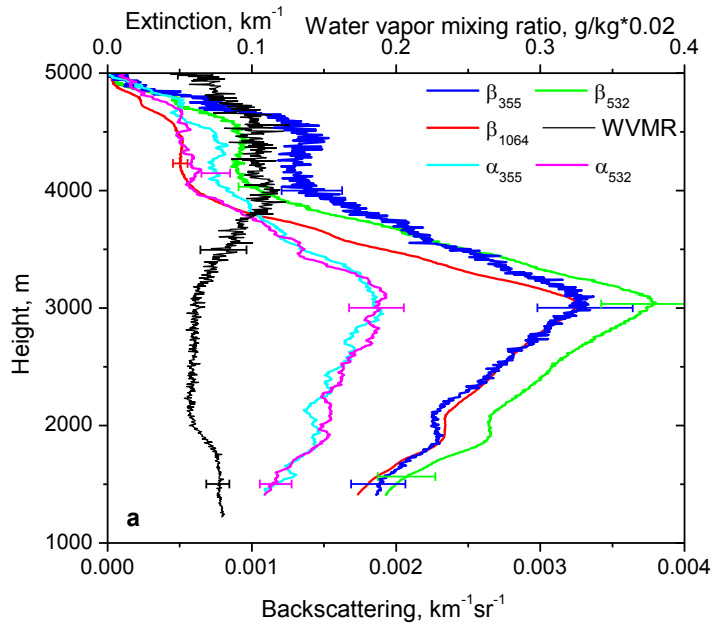
2

3

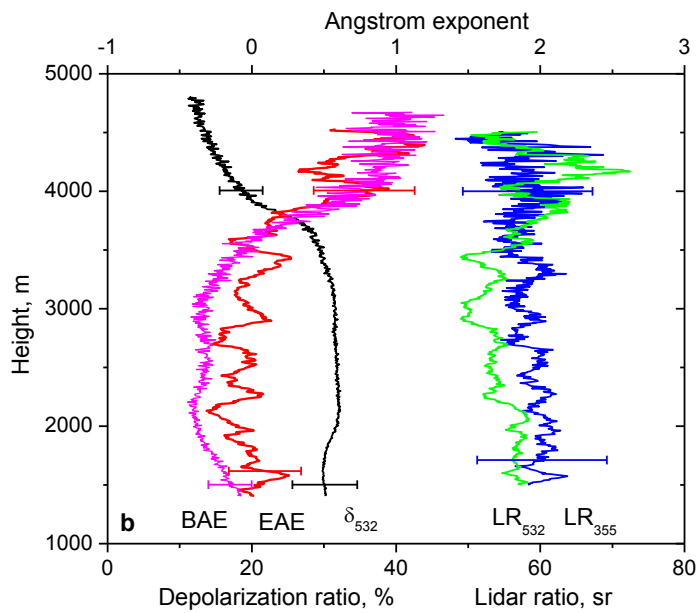
4 Fig.14. Five-day backward trajectories for the air mass in Mbour at altitudes 2000 m, 3000 m,  
5 4500 m on 10 April 2015 at 01:00 UTC.

6

1



2



3

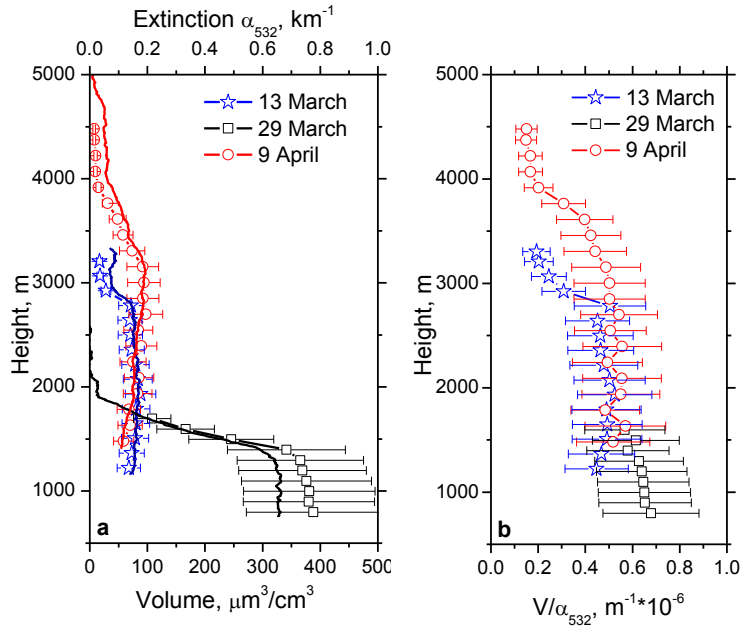
4

5 Fig.15 Vertical profiles of (a) backscattering and extinction coefficients and (b) depolarization  
6 ratio, backscattering and extinction Ångström exponents at 355/532 nm measured on 10 April  
7 2015 for period 00:00-02:00 UTC.

8

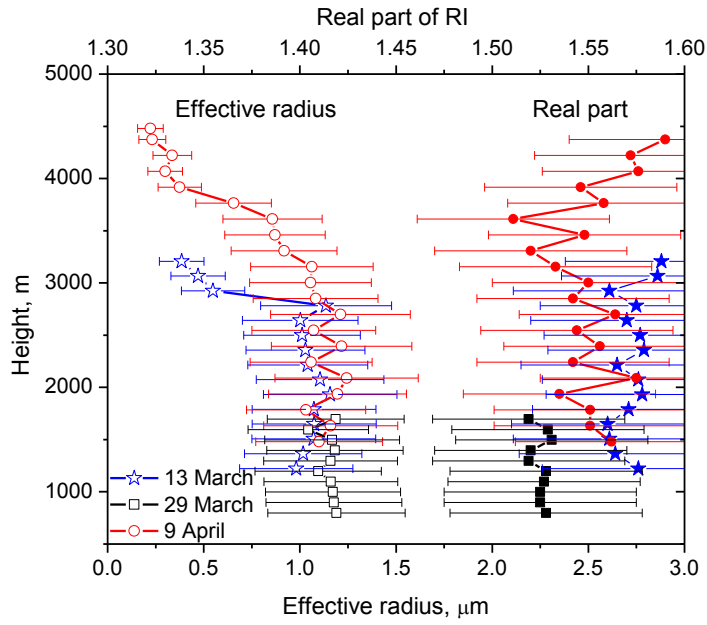


1  
2  
3

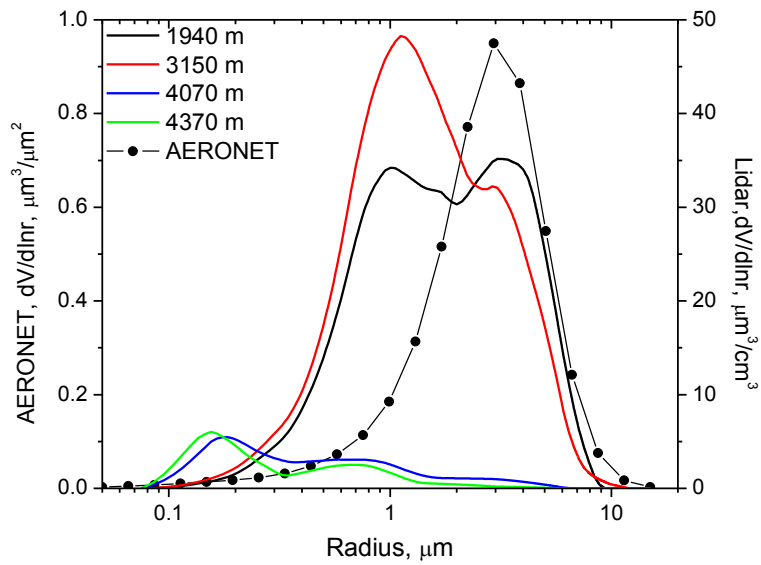


4 Fig.16. (a) Vertical profiles of the particle volume density  $V$  (symbols) retrieved from  $3\beta+2\alpha$   
5 measurements on 13 March, 29 March and 10 April. Solid lines indicate the profiles of  
6 extinction coefficient at 532 nm. (b) Volume – extinction ratio  $V/\alpha_{532}$  for the days considered.

7



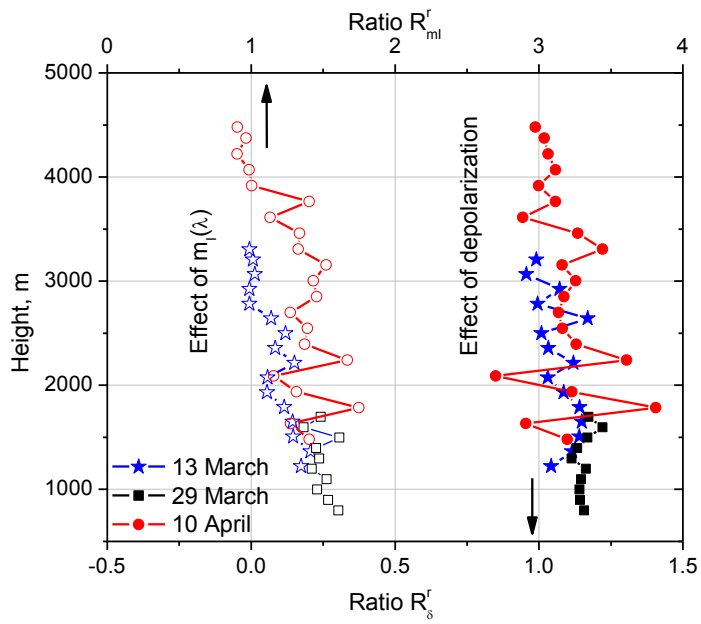
1  
 2 Fig.17. The profiles of (open symbols) the particle effective radius and (solid symbols) the real  
 3 part of RI retrieved from  $3\beta+2\alpha$  measurements on 13 March, 29 March and 10 April.



1  
 2 Fig.18. Particle size distributions retrieved from the measurements on 10 April for four height  
 3 layers 1940, 3150, 4070, 4370 m. Symbols show the PSD provided by AERONET on 9 April at  
 4 18:00 UTC, inversion level 1.5.

5

1



2

3 Fig. 19. Enhancement of retrieved effective radius due to using the particle depolarization ratio  
4 in input data set ( $R_{\delta}^r$ ) and due to accounting for the spectral dependence of the imaginary part of  
5 RI ( $R_{ml}^r$ ). Shown are results for the measurements on 13 March, 29 March and 10 April 2015.